Driving Saturn's magnetospheric periodicities from the upper atmosphere/ionosphere

Xianzhe Jia,[1] Margaret G. Kivelson,[1,2] and Tamas I. Gombosi[1]

[1]   Saturn's magnetospheric structure and the intensity of radio frequency emissions from its immediate surroundings are modulated at close to the planet's rotation period. Analogous rotation-modulated variations at Jupiter are readily interpreted as effects of the non-axisymmetric intrinsic magnetic field. At Saturn, to the contrary, the high level of axial symmetry in the intrinsic field suggests that the periodicity is not internally imposed. A number of mechanisms have been proposed to account for the observations. Each model explains a subset of the observations in a qualitative manner, but no quantitative models yet exist. Here, using a magnetohydrodynamic simulation, we investigate the magnetospheric perturbations that arise from a localized vortical flow structure in the ionosphere near 70° S-latitude that rotates at roughly the rate of planetary rotation. The model reproduces nearly quantitatively a host of observed magnetospheric periodicities associated with the period of the dominant (southern) radio frequency emissions during the Cassini epoch including rotating, quasi-uniform magnetic perturbations in the equatorial plane, rotating mass density perturbations, periodic plasmoid releases that we associate with observed bursts of energetic neutral atoms (ENAs), periodic oscillations of magnetospheric boundaries, current sheet flapping, and periodic modulation of the field-aligned currents linked to Saturn's kilometric radiation (SKR). The model is not unique but is representative of a class of models in which asymmetric flows in the (as yet unmeasured) upper atmosphere couple to the ionosphere and generate currents that flow into the magnetosphere. It can be extended to include the second periodicity that has been associated with SKR emissions in the northern hemisphere.

1.   Introduction

[2] At orbital distances of 5 AU and beyond, the low dynamic pressure and weak interplanetary magnetic field of the solar wind (down by an order of magnitude or more relative to values near Earth) interact with the strong planetary magnetic fields of the rapidly rotating giant planets, Saturn and Jupiter, to create magnetospheres that dwarf Earth's magnetosphere. In these distant magnetospheres, the role of the solar wind in driving dynamics is secondary to that of internal processes. Electrical currents that flow from the ionospheres of these rapidly rotating planets to their magnetospheres impose strong forces on the near equatorial plasma [e.g., *Vasyliũnas*, 1983; *Gombosi et al.*, 2009]. Correspondingly, magnetospheric responses develop that lack a terrestrial counterpart. Here we put forward a model that accounts for a class of phenomena linked to planetary

rotation that are observed at Saturn and are possibly present at Jupiter but are not found in Earth's slowly rotating magnetosphere.

[3] At both planets, currents coupling the magnetosphere and the ionosphere generate radiation in the radio frequency band (decametric for Jupiter, kilometric for Saturn). Jupiter's decametric radiation, discovered in the mid-1950s [*Shain*, 1955; *Burke and Franklin*, 1955], varies in intensity at a period that remains constant to within the error of the observations [*Yu and Russell*, 2009]. The period was, from the start, accepted as the period of Jupiter's rotation [e.g., *Carr et al.*, 1958]. Saturn's kilometric radiation (SKR) varies in intensity at approximately the rotation period of the cloud tops [*Warwick et al.*, 1981] and, with Jupiter as an example, it was natural to believe that the periodic intensification was governed by the rotation of the deep interior [*Desch and Kaiser*, 1981]. Consequently, the SKR period was adopted by the International Astronomical Union (IAU) as the planetary rotation period [*Carr et al.*, 1981; *Seidelmann et al.*, 2002], and rotation phase was taken to represent planetary longitude. The SKR source has been shown to rotate with the planet, but to vary in intensity, with a peak of radiation power observed as the source passes through the morning sector [*Lamy*, 2011]. By convention,

---

[1]Department of Atmospheric, Oceanic and Space Sciences, University of Michigan, Ann Arbor, Michigan, USA.
[2]Department of Earth and Space Sciences, University of California, Los Angeles, California, USA.

the phase of the subsolar meridian is defined as 100° at the maxima of a sinusoidal fit to the SKR power [*Desch and Kaiser*, 1981; *Kurth et al.*, 2007].

[4] At fixed locations within the two magnetospheres, plasma and field properties also vary at roughly the radio period yet, despite the apparent similarity of the two systems, it has become clear that their periodicities must be driven differently. At Jupiter the periodicity is accounted for by asymmetry of the planetary magnetic field, which is tilted by ~10° relative to the spin axis [*Smith et al.*, 1975; *Connerney*, 1993]. The observed temporal modulation arises directly from the rotation of the tilted dipole moment. Saturn's intrinsic magnetic field, on the other hand, has thus far revealed no axial asymmetries, the tilt of its dipole having recently been shown to be less than 0.1° [*Burton et al.*, 2010; *Cao et al.*, 2011]. Thus the periodicity revealed by particles and fields in Saturn's magnetosphere [*Espinosa and Dougherty*, 2000; *Espinosa et al.*, 2003; *Paranicas et al.*, 2005; *Carbary et al.*, 2007a, 2008; *Southwood and Kivelson*, 2007; *Andrews et al.*, 2008, 2010; *Burch et al.*, 2009; *Mitchell et al.*, 2009a; *Provan et al.*, 2009a, 2009b; *Brandt et al.*, 2010] must have a source other than dipole tilt.

[5] Additional aspects of the SKR periodicity constrain plausible mechanisms for its origin. The period at which its power is modulated drifts at a rate that can be as great as ~1% per year [*Lecacheux et al.*, 1997; *Galopeau and Lecacheux*, 2000; *Gurnett et al.*, 2005; *Zarka et al.*, 2007; *Kurth et al.*, 2007, 2008], an observation that rules out a source inside the planet because the rotation rate of a body as massive as Saturn cannot change so rapidly [*Stevenson*, 2006]. It is also not plausible for high order magnetic anomalies to drift fast enough to account for such large shifts. Furthermore, the periods of electromagnetic properties differ in the northern and southern hemispheres and appear to vary with Saturn's seasons [*Gurnett et al.*, 2009b, 2010; *Ye et al.*, 2010; *Lamy*, 2011; *Southwood*, 2011], an additional challenge to interpretation of their origin.

[6] If the source of the periodicity is not internal to Saturn, the rotating features must arise from an azimuthal structure either in the magnetosphere or in the upper atmosphere. Some models suggest that the periodicity is driven by spontaneously broken symmetry of the convective flows in the equatorial region of the magnetosphere [*Goldreich and Farmer*, 2007; *Gurnett et al.*, 2007; *Burch et al.*, 2009] or by intermittent dayside reconnection [*Burch et al.*, 2008]. We understand that convective flows with appropriate symmetry will impose periodicities on many properties of the magnetosphere, but we find this type of model inconsistent with magnetometer observations that we discuss below. We also note that the averaged phase of the SKR variation drifts very slowly, i.e., at a rate established by the changing period. This near-constancy of phase appears to us to present a problem to any convective flow model because one expects that the rotation rate of magnetospheric plasma will undergo dramatic changes as the magnetosphere changes scale in response to interplanetary shocks or rotations of the interplanetary field (see for example, the global simulations of *Hansen et al.* [2000] and *Fukazawa et al.* [2007]). (Magnetospheric compressions and expansions change the angular velocity of confined plasma as a consequence of angular momentum conservation.) We prefer to attribute the periodicity to a source of broken symmetry in the upper atmosphere.

[7] The upper atmosphere is a region with inertia intermediate between that of the deep interior and of the magnetosphere that, despite fluctuating properties of the solar wind [*Zarka et al.*, 2007], could plausibly maintain a close-to-constant rotation rate with modest seasonal variations. In order to impose periodicities onto the magnetosphere, the asymmetric features of the upper atmosphere must couple to the ionosphere and generate field-aligned currents (FACs). The seasonal dependence of SKR periodicities, the problems associated with other possible sources of the modulation, and the plausible link to the seasonally varying atmosphere/ionosphere and to zonal wind structure have been noted previously [*Gurnett et al.*, 2009a, 2009b, 2010; *Mitchell et al.*, 2009a; *Southwood and Kivelson*, 2009] but have not been pursued quantitatively. New in this work is the development of an explicit quantitative model of the periodic behavior of the magnetosphere. We start by invoking vortical flow within the ionosphere, maintained in its motion through coupling to the upper atmosphere. Vortical flow in the ionosphere generates FACs, and the rotation of a region of perturbed flow around the spin axis imposes periodicity on the magnetosphere. Indeed, *Smith* [2006, 2011] has shown that asymmetric heating of Saturn's thermosphere sets up vortices that drive currents into the magnetosphere. He has achieved considerable success in producing a periodically varying current system, far weaker than, yet similar in structure to, that present in the magnetosphere, but his model is not designed to investigate the diverse periodic phenomena that develop in the magnetosphere. In this work, we seek to establish what periodic magnetospheric features can be accounted for by the ionospheric vortex model by carrying out a global magnetohydrodynamic (MHD) simulation in which a flow vortex in the ionosphere rotates about the planetary spin axis at a fixed period. We note that although MHD does not treat kinetic aspects of the plasma system (e.g., particle drift physics), only an MHD model can provide insight into large-scale behavior of the magnetospheric system. Since the focus of this work is global responses of the coupled ionosphere/magnetosphere/solar wind system, MHD simulation is the appropriate tool for investigating the problem of interest. As the simulation is computationally intensive, we have not initially tested multiple forms of the vortical flow structure, but have selected a form that incorporates the dominant symmetry of observed perturbations. The objective of our work is to provide a "proof of principle" by demonstrating that the model reproduces most of the periodicities observed in Saturn's magnetosphere and ionosphere with nearly quantitative fidelity.

[8] In the MHD simulation, the vortical flow structure imposed on the ionosphere is set in rotation at a fixed period (10.8 h) corresponding to the southern SKR periodicity. The perturbation is not frozen into the ionosphere, which rotates at a slower rate because of magnetospheric drag. Conceptually, we envision that the vortical flows are embedded in upper atmosphere winds that rotate more slowly than the tropospheric clouds [*Sánchez-Lavega et al.*, 2004] but somewhat faster than the ionosphere itself. Efficient eddy diffusion or analogous processes are required to propagate the momentum of the atmospheric flow into the ionosphere. Although the model imposes a defined periodicity on the magnetosphere, it is not evident *ab initio* that it can account for the numerous, periodic plasma and field signatures that have been reported

and that are summarized in Section 3. Thus, it is the purpose of this work to extract from the simulation the periodic magnetospheric responses to the assumed driver and to compare them with Cassini measurements.

[9] In section 2 we describe the MHD model used to test the hypothesis of this paper. For this initial study, we have focused on the magnetospheric phenomena linked to a southern hemisphere source rotating at the period of the southern source near solstice. We embed the magnetosphere in a steady solar wind with a southward-oriented interplanetary magnetic field in order to minimize solar wind disturbances and to assure that the time-varying phenomena present in the magnetosphere are internally driven. The ionospheric vorticity is imposed in a mathematically tractable form whose symmetry has the characteristics desired. Section 3 presents the results of the simulation and compares them with observations of periodic phenomena. Section 4 compares features of the model studied with expectations from other models of the source of the periodicities. Section 5 reviews the aspects of magnetospheric periodicity that are accounted for by our model in its initial runs and describes augmentations contemplated for further development.

2.   The Model

[10] We model Saturn's magnetosphere by using the global, 3D MHD model BATSRUS (Block Adaptive Tree Solar wind Roe-type Upwind Scheme) [*Powell et al.*, 1999; *Gombosi et al.*, 2002, 2004] together with an Ionosphere Electrodynamics (IE) solver [*Ridley et al.*, 2004]. BATSRUS has previously been used to model Saturn's magnetosphere [*Hansen et al.*, 2000, 2005; *Gombosi and Hansen*, 2005; *Zieger et al.*, 2010]. In the following we introduce the model basics and input parameters.

2.1.   Model Basics

[11] BATSRUS solves the governing MHD equations (conservation of mass, momentum and energy together with Faraday's law) with a near-conservative finite-volume method [*Powell et al.*, 1999; *Gombosi et al.*, 2004]. BATSRUS has been adapted to model Saturn's magnetosphere by including mass-loading source terms in the MHD equations (for details see *Hansen et al.* [2000]) and further improved by adjusting the spatial distribution of internal plasma sources as well as the mass-loading rates according to recent observations [*Hansen et al.*, 2005]. The main plasma source of water group ions W^+ (H_2O^+, OH^+, O^+, H_3O^+) originating from Enceladus and the rings is included in our global model as an axisymmetric disc-like source centered at ~5.35 R_S (R_S, radius of Saturn = 60268 km) [*Richardson et al.*, 1998], while a secondary plasma source of nitrogen ions N^+ originating from Titan is included as an axisymmetric torus around Titan's orbit at ~20 R_S. Estimates of the total H_2O production rate range from $\sim5.0 \times 10^{27}$ ions/s (or ~150 kg/s) [*Fleshman et al.*, 2010] to $\sim10^{28}$ ions/s (or ~300 kg/s) [*Jurac and Richardson*, 2005; *Hansen et al.*, 2006; *Burger et al.*, 2007; *Cassidy and Johnson*, 2010]. From Cassini INMS measurements, *Smith et al.* [2010] reported that the net H_2O production rate at Enceladus varies significantly from pass to pass, ranging from <72 kg/s during the E2 flyby to ~750 kg/s during the E5 flyby. A large fraction of the neutrals escape the Saturnian system without being ionized, but some are ionized within the magnetosphere through photoionization or electron impact ionization [*Jurac and Richardson*, 2005]. Assuming that $\sim10\%$ [*Fleshman et al.*, 2010] to 30% [*Jurac and Richardson*, 2005] of the neutrals are ionized, one obtains a net plasma addition rate ranging from ~10 kg/s to 220 kg/s. We use a nominal total mass-loading rate of $\sim6 \times 10^{27}$ /s for W^+ and $\sim5 \times 10^{25}$ /s for N^+, corresponding to a total mass-loading rate of plasma of ~170 kg/s assuming an average mass of 16.6 amu for W^+ and 14 amu for N^+, a source rate within the range of estimated rates. In addition to the mass-loading source term, we also include in our MHD model the source term associated with charge-exchange, a process that does not add mass to the system but affects the momentum and energy exchange of the plasma system by converting hot ions into fast neutrals and replacing them with cold ions. As suggested by *Richardson et al.* [1998], the dominant charge-exchange reaction in Saturn's magnetosphere is the symmetric charge-exchange between O and O^+. The charge-exchange rate in our model is computed based on the results of *Richardson et al.* [1998] that provide information about the oxygen neutral density (peaks at ~4 R_S) and the reaction rate. The total charge-exchange rate used in the present run is ~70 kg/s.

2.2.   Inner Boundary Conditions: Coupling Between BATSRUS and IE

[12] In our model, the coupling of the global magnetosphere and the ionosphere is handled through FACs in a simplified way that is used in most Earth magnetosphere models [*Raeder et al.*, 1998; *Ridley et al.*, 2004; *Tóth et al.*, 2005; *Lyon et al.*, 2004; *Hu et al.*, 2007]. Field-aligned currents are calculated in the magnetosphere at 4 R_S, about 1 R_S beyond the inner boundary of the magnetospheric domain, and then mapped into the ionosphere at ~1 R_S along dipole field lines. Owing to the continuity of electric currents, field-aligned currents must close through horizontal currents in the ionosphere, which is approximated by a height-integrated resistive layer located at ~1000 km above the 1 mbar level. Closure currents in the ionosphere are then used to derive the distribution of the electric potential using a Poisson solver in the IE model and, in turn, the ionospheric convection pattern for a given distribution of ionospheric conductance (including both Pedersen and Hall conductances). The calculated convection modulation is then superimposed onto the rigid corotation flow for a given rotation rate of the planet to obtain a modified ionospheric plasma transport. Finally, the ionospheric convection pattern, which determines the flow velocity perpendicular to the magnetic field, is mapped back along dipole field lines from the ionosphere to the magnetosphere under the ideal MHD assumption that magnetic field lines are equipotentials. The mapped flows, therefore, set the transverse velocity components at the inner boundary of the global MHD model. In addition, we take as an inner boundary condition a mass density of 0.1 amu/cm^3 and a temperature of 3 eV and fix these conditions at the magnetospheric inner boundary (at 3 R_S). The planetary rotation period is set as 648 min (or 10.8 h), consistent with the southern SKR period for late 2005 and early 2006 [*Gurnett et al.*, 2009b]. We assume a rigidly rotating thermosphere that can deliver momentum sufficient to maintain steady ionospheric vorticity throughout the simulated interval.
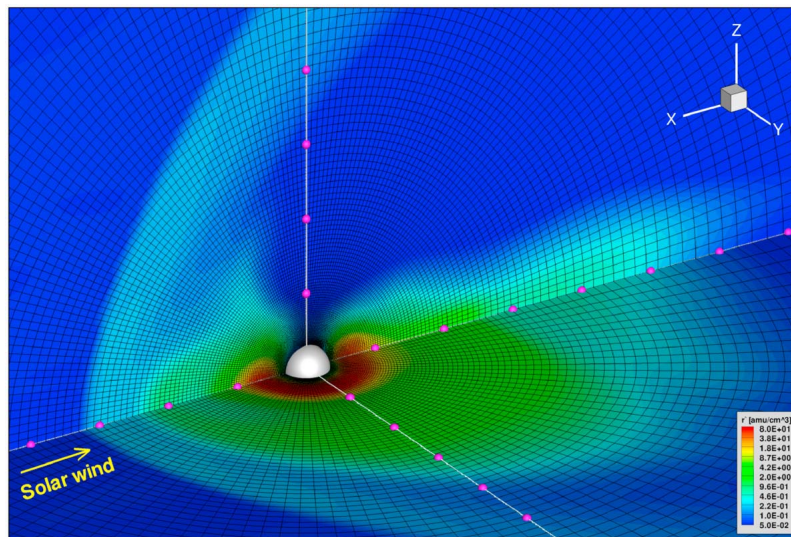
Figure 1. A typical grid distribution in two cuts through a portion of the 3D spherical mesh used in our simulation (viewed from the upstream flank side). These two planes respectively correspond to the XY plane (at Z = 0) and the XZ plane (at Y = 0) in the Kronocentric Solar Magnetospheric (KSM) coordinates, where +X points toward the Sun, +Y is perpendicular to the dipole axis (the latter is aligned with the rotation axis in the case of Saturn) and points toward dusk, and +Z is chosen so that the dipole or rotation axis lies in the XZ plane. For the model runs of this paper, the dipole axis is taken perpendicular to the flow, hence aligned with Z. Color contours of plasma density are plotted; they reveal magnetospheric boundaries, such as the magnetopause and the bow shock. The three Cartesian axes are labeled with magenta balls every 10 R_S. Also plotted is a white sphere of radius 3 R_S, which corresponds to the inner boundary of the global magnetosphere model.

[13] In addition to the FACs derived from the global magnetosphere model, the ionospheric conductance is a required input parameter in the IE model. At Saturn, the ionospheric conductance is quite uncertain. Estimates of the ionospheric Pedersen conductance, mainly based on Voyager era radio occultations and modeled ionospheric electron density profiles, vary widely from 0.1 S to 100 S [*Connerney et al.*, 1983; *Atreya et al.*, 1984; *Cheng and Waite*, 1988]. Recent estimates from calculations using Cassini RSS measurements [*Moore et al.*, 2010] and theoretical studies [*Bunce et al.*, 2003; *Cowley et al.*, 2008] using magnetospheric flow measurements together with auroral observations suggest an ionospheric Pedersen conductance of several Siemens. Here we set the Pedersen conductance to 1 S in the northern ionosphere and 3 S in the southern hemisphere to represent the southern summer season. The Hall conductances in the two ionospheres are set to be zero for simplicity.

2.3. Simulation Grid and Coordinate System

[14] BATSRUS has the capability to use generalized curvilinear coordinates, which provide a smooth mapping from a logically Cartesian grid to an arbitrary curvilinear grid, including spherical, cylindrical and toroidal grids [*Tóth et al.*, 2012]. Our present model adopts a high-resolution non-uniform spherical grid that enables us to resolve fine structures of the large-scale magnetospheric currents responsible for the coupling between the magnetosphere and ionosphere. Figure 1 shows a typical grid distribution in two cuts (equatorial and meridional) through a portion of the 3-D spherical mesh used in our model. The spherical grid used here provides fine resolution in regions of interest such as

the inner magnetosphere and the magnetospheric boundaries (such as the bow shock and the magnetopause). The grid resolution around the main mass-loading region associated with Enceladus' neutral cloud reaches ~0.2 R_S (between 5 and 10 R_S) and increases to 0.5 R_S near Titan's orbit (at ~20 R_S). In addition, a high-resolution grid with 0.5° resolution in latitude (θ) and 1° resolution in longitude (ϕ) is adopted for the IE solver.

[15] Although we use a spherical grid system in order to achieve high resolution in regions of interest, the set of MHD equations is still solved in a Cartesian simulation box. In order to include as much of Saturn's magnetosphere and the magnetotail as possible at an acceptable computational cost, we set a rectangular computational domain (in which the set of MHD equations is solved) covering the region $-576\ R_S < X < 96\ R_S$, $-192\ R_S < Y$, $Z < 192\ R_S$, where X, Y, and Z are the Kronocentric Solar Magnetospheric (KSM) coordinates with + X pointing toward the Sun, +Y oriented perpendicular to the dipole axis (which is aligned with the rotation axis in the case of Saturn) and pointing toward dusk, and +Z chosen so that the dipole (and rotation) axis lies in the XZ plane. In order to avoid the high Alfvén speed close to the planet that greatly limits the allowable time step in the simulation, the inner boundary of the global magnetosphere model is placed at a radial distance of 3 R_S. In the present study, Saturn's rotation and dipole axes are placed along the Z axis in KSM coordinates and the incident solar wind flow is antiparallel to the *x* axis. A centered internal dipole with equatorial surface strength of 20800 nT is used to represent Saturn's internal magnetic field [*Dougherty et al.*, 2005].
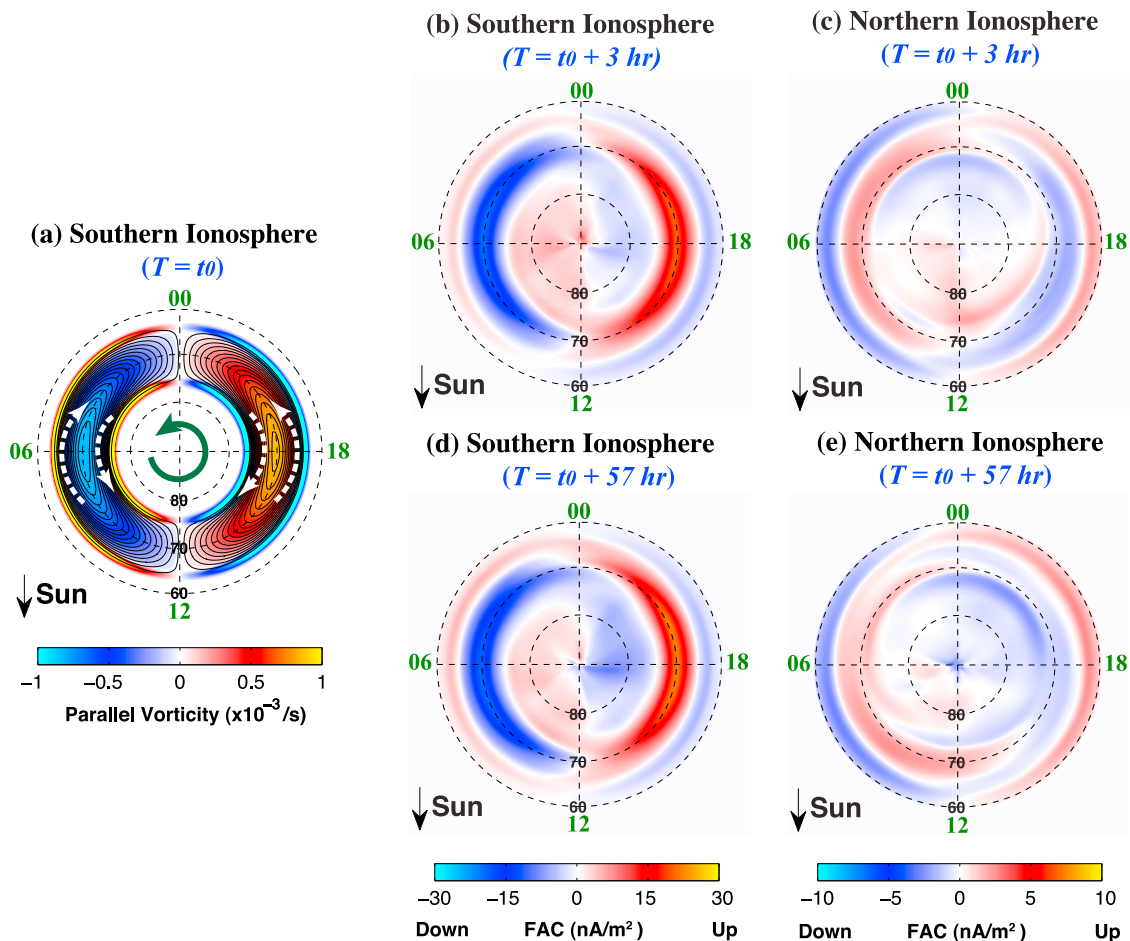
Figure 2. Ionospheric conditions in the northern and southern hemispheres from the simulation that imposes a vortical flow perturbation. (a) The imposed flow vortex in the southern hemisphere (at $T = t_0$) obtained from one cycle of a spherical harmonic potential of order $\ell = 15$, $m = 1$. Color indicates the flow vorticity parallel to the local magnetic field, solid lines are flowlines and dashed arrows show local flow directions. No vortical flow is imposed in the northern ionosphere. The vortices are fixed in the rotating system and rotate counterclockwise relative to LT (as shown by the green circular arrow). (b and c) Color contours of field-aligned current density associated with the perturbed flow in the southern and northern ionosphere, respectively, from early (at $T = t_0 + 3$ h) in the simulation. (d and e) Same as Figures 2b and 2c but at the same rotation phase 50 rotations later at time $T = t_0 + 57$ h. Note that the weak northern hemisphere field-aligned currents are shown with a different color bar. The views of both hemispheres are downward from the north. Dashed black circles are at fixed latitudes separated by $10°$.

2.4. Ionospheric Flow Vortex Model

[16] Previous simulations of Saturn's magnetosphere have examined the interaction of a uniformly rotating inner boundary [*Hansen et al.*, 2000; *Fukazawa et al.*, 2007] or ionosphere [*Hansen et al.*, 2005; *Zieger et al.*, 2010] with the magnetosphere. In our simulation, the electric potential corresponding to magnetospheric flow at each time step is mapped along field lines into the ionosphere. In the ionosphere we add the electric potential corresponding to a perturbation flow driven by collisions with the upper atmosphere. It is this imposed perturbation that we model as a localized flow vortex in the southern ionosphere rotating about the spin axis with a bulk rotation period fixed at 10.8 h. We specify a mathematically tractable form of the vortical flow by using spherical harmonics to represent the electric potential (or, equivalently, the flow streamlines) in the ionosphere. Thus, in the southern ionosphere we impose a vortical flow perturbation along the equipotentials of the spherical harmonic $Y_{15,1}(\theta, \phi)$ limited to one cycle in latitude (θ) centered at $70°$ for all longitudes (ϕ) (see Figure 2a). The choice of this specific spherical harmonic is based on the fact that the magnetic perturbations observed have an $m = 1$ symmetry in the rest frame of the planet and that the cam currents driving the magnetospheric perturbations flow near $70°$ invariant latitude [*Southwood and Kivelson*, 2007]. The perturbation flow is selected to have finite vorticity because vorticity in a magnetized plasma drives FACs. The magnitude of the vorticity (color contours of Figure 2a) is set to reproduce the amplitude of magnetic perturbations observed in the equatorial magnetosphere near ~12 R_S. The corresponding ionospheric flow speeds range from ~0.3 km/s near $70°$ latitude to ~3.0 km/s near $65°$ and $75°$ latitudes. Such flow speeds are within the range of zonal wind speeds

in the high latitude thermosphere suggested by a global circulation model of Saturn's thermosphere [*Müller-Wodarg et al.*, 2006] that takes into account Joule heating in the high latitude auroral region.

2.5. Upstream Solar Wind Input

[17] In order to focus on the effects of the assumed ionospheric flow anomaly, we run a generic version of our MHD simulation with steady solar wind input and an interplanetary magnetic field (IMF) orientation that minimizes dynamical interactions with the magnetospheric magnetic field. The solar wind velocity is set to 400 km/s perpendicular to the dipole axis and the IMF to 0.5 nT southward. The solar wind plasma density is set to 0.05 amu/cm^3 and the plasma temperature is 20 eV.

2.6. Model Initialization

[18] Before introducing the flow vortex in the global model, we first create a baseline magnetosphere under the steady solar wind conditions described above. The baseline magnetosphere is obtained by first running the model under an iterative "local time stepping" mode [*Ridley et al.*, 2002] for over 15000 iterations followed by advancing the code in a time-accurate mode for ~100 h, a time that we designate as t_o. At this time we turn on the flow vortex model and continue to run for another ~50 h to allow the simulation to stabilize. Thus the results that we show in the following sections are taken from time steps later than 150 h of simulation time.

3. Magnetospheric Periodicities: Comparison of Model and Observations

[19] Periodic magnetospheric variations have been found in currents, in rotations and compressions of the magnetic field, in particle distributions and in boundary locations. Most of these modulations were discovered in studies of data from the Cassini Orbiter. However, shortly before Cassini arrived at Saturn, and almost two decades after periodic modulation of SKR power [*Desch and Kaiser*, 1981] and energetic particle fluxes [*Carbary and Krimigis*, 1982] were discovered, *Espinosa and Dougherty* [2000] and *Espinosa et al.* [2003] reported that Pioneer and Voyager magnetometer data showed periodic field variations with structure that require a source external to the planet. Cassini measurements confirmed the presence of a pattern of rotating magnetic perturbations quasi-uniform near the equator inside of ~12 R$_S$ [*Southwood and Kivelson*, 2007; *Andrews et al.*, 2008, 2010]. Also observed were a rotating asymmetric ring current [*Krimigis et al.*, 2007; *Provan et al.*, 2009a; *Andrews et al.*, 2010; *Brandt et al.*, 2010]; a rotating field-aligned current system (the "cam current") that flows between the southern and northern ionospheres near 70° invariant latitude and varies in amplitude and direction roughly sinusoidally with longitude [*Southwood and Kivelson*, 2007]; rotating density enhancements [*Gurnett et al.*, 2007; *Burch et al.*, 2008]; periodic displacements of the magnetotail current sheet beyond ~15 R$_S$ [*Arridge et al.*, 2008b, 2011; *Khurana et al.*, 2009; *Provan et al.*, 2012]; periodic plasmoid releases in the magnetotail [*Burch et al.*, 2008; *Mitchell et al.*, 2009a; *Jackman et al.*, 2009]; bursts of energetic neutral atoms (ENAs) arising from periodic

plasma injections into the middle magnetosphere [*Paranicas et al.*, 2005; *Carbary et al.*, 2008; *Mitchell et al.*, 2009a]; and periodic displacements of the magnetopause and bow shock [*Clarke et al.*, 2010a, 2010b]. These are among the plasma and field phenomena observed in the magnetosphere that require explanation and that we seek to extract from the MHD model described in Section 2.

3.1. The Magnetosphere-Ionosphere Current System

[20] The vortical flows imposed in Saturn's southern ionosphere in our simulation are illustrated in the rotating frame at time t_o in Figure 2a; color represents parallel vorticity. This structure is set into rotation with a rotation period of 10.8 h, a period that we shall refer to as the rotation period. No flow is imposed on the northern ionosphere. Plasma flowing at velocity **v** in a magnetic field, **B**, implies the presence of an electric field, $\mathbf{E} = -\mathbf{v} \times \mathbf{B}$. The electric field is directed toward the center of the vortex on the left side of Figure 2a and outwards from the center of the vortex on the right side. The electric field in turn drives current, $\mathbf{j} = \sigma\mathbf{E}$, where σ is the ionospheric Pedersen conductivity. Where the ionospheric currents converge, FACs flow upward from the ionosphere; where the ionospheric currents diverge, FACs flow downward into the ionosphere from the magnetosphere. The FACs present 3 h after the imposition of vorticity are shown in Figures 2b and 2c. Some of the FAC generated in the southern ionosphere flows through the magnetosphere and into the northern ionosphere where it can be identified as a FAC-region of opposite polarity centered close to 70° latitude. The color scales have been stretched by a factor of 3 in the plot for the northern hemisphere where the current intensity is much reduced, indicating that most of the current driven by the southern hemisphere vortex closes through currents perpendicular (to **B**) diverted within the near-equatorial magnetosphere. Weak FACs present in the polar cap in both north and south are primarily generated in the magnetosphere. After the simulation has been run for 50 more hours, at t_0 +57 h, the system stabilizes in the sense that the variations become periodic at the rotation period. Figures 2d and 2e show typical distributions of FACs flowing into and out of the two ionospheres at this later time. The driven currents in the south have changed little from their initial form, but in the north they have become more diffuse. The magnetosphere imposes a drag on both ionospheres, especially in the polar regions where the currents have intensified considerably. Magnetospheric drag implies that the ionosphere is sub-corotating. Below we discuss how the currents vary over a rotation after the system has fully stabilized.

3.2. Magnetic Perturbations in and Across the Equatorial Plane

[21] In the magnetosphere, the rotating current system produces diverse periodic perturbations. In Figure 3 we show the magnetic perturbation vectors ($\Delta\mathbf{B}$) in the equatorial plane at different rotation phases as obtained from Cassini magnetometer measurements by *Andrews et al.* [2010] (left in each pair) and from the simulation (right). [The data are represented in a spherical coordinate system, r, θ, ϕ, with angles measured relative to the spin axis and vector lengths proportional to $(\Delta B_r^2 + \Delta B_\phi^2)^{1/2}$.] The similarity of the pairs of plots is striking. Perturbation field
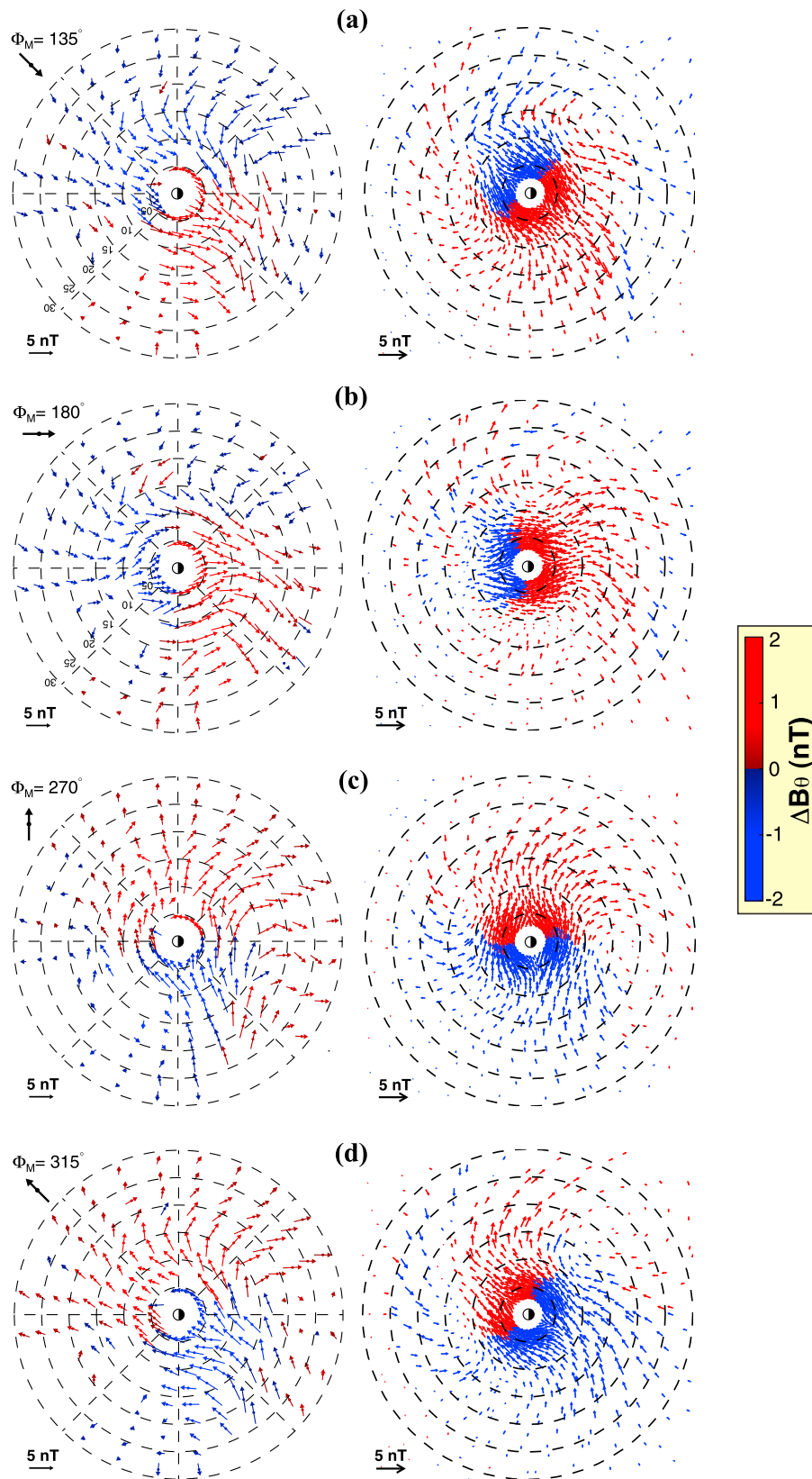
Figure 3

magnitudes and orientations are similar. Inside of $\sim$10 R_S the perturbation field is almost uniform in the direction of the phase arrow shown in the data plot, with diversion around the inner boundary. Outside of $\sim$10 R_S the field twists, with the twist more evident in some local time sectors than in others. In the simulation, the transverse field perturbations are accompanied by antiparallel flow perturbations.

[22] Figure 3 gives a global view of the magnetic perturbations near the equator but does not show how the transverse perturbations vary in the north-south direction across the equatorial magnetosphere. North-south structure is of special interest because it reveals something about the way in which the perturbations are imposed. Consider, for example, the magnetic perturbation that would be imposed by a radially outward convective flow near the equator. In Figure 4, we show magnetic field lines distorted by an azimuthal flow concentrated near the equator (Figure 4a) or a radial outflow concentrated near the equator (Figure 4b). The effect of such localized flows is to stretch the equatorial portion of the flux tube, producing a positive $\Delta\mathbf{B}_\perp$ above the north-south center of the flow and a negative $\Delta\mathbf{B}_\perp$ below or vice versa. The signature is likely to be clearer in ΔB_ϕ than in ΔB_r because the stretching of the background field implies that ΔB_r always reverses across the equator. Thus, spacecraft measurements on an orbit that cuts south-north through the equator should encounter a node at or near the equator in ΔB_ϕ unless the equator crossing occurs fortuitously at the zero of its variation with SKR phase.

[23] An example of the variation of the perpendicular components of the perturbation field across the equator on a Cassini orbit is plotted in Figure 4, which also includes traces extracted along the spacecraft orbit from the simulation. As the time resolution of the simulation output is 1 h, the simulated trace misses rapid changes over short time scales, but otherwise tracks the data relatively closely except very near closest approach. The magnetic cycle is clearest in the ΔB_ϕ trace. Vertical black lines in the bottom panel of Figure 4c mark half a cycle (Doppler shifted [*Cowley et al.*, 2006; *Arridge et al.*, 2011]) of rotation during which ΔB_ϕ increases to near its maximum amplitude at the equator and shows no evidence of a change of sign as the spacecraft crosses the equator. It is hard to make the case that the oscillatory variation in this component is produced by an equatorial flow pattern. On the other hand, the simulation (driven from the lower end of the flux tube) shows the oscillation in much the form measured on this orbit.

[24] The field vectors in Figure 3 are colored to indicate the sign of the θ-component of the magnetic perturbation. Over most of the plane, ΔB_θ is positive where ΔB_r is positive and vice versa. The limited regions where the products are negative are localized near boundaries between negative and positive ΔB_θ. The locations of those boundaries differ

slightly in the model and the data. The discrepancy can be attributed to the fact that the model was run with the solar wind flow vector orthogonal to the spin axis, which imposes an unrealistic north-south symmetry to the system, whereas the data were acquired between 2004 and 2007, near solstice when the oblique flow of the solar wind introduced a north-south asymmetry that distorted the magnetic equator into a bowl shape [*Arridge et al.*, 2008a]. The product, $\Delta B_\theta \bullet \Delta B_r/\mu_o$, which is on average positive both in the model and in the data, gives insight into the source of the periodic perturbations because it is the element of the Maxwell stress tensor, $T_{\theta\ r}$ that characterizes the flux of electromagnetic momentum parallel to the r axis crossing a surface normal to the θ axis per unit time. This point was brought to the attention of the authors by *David Southwood* [personal communication, 2011]. A positive value of the divergence of $T_{\theta\ r}$ indicates that momentum flux in the θ direction is negative, i.e., directed northward, and thus consistent with a source of momentum to the south of the equator. If the source is ionospheric, the sign of $T_{\theta\ r}$ identifies the hemisphere in which momentum is introduced. Although we have not yet run a full simulation with sources present simultaneously in both northern and southern ionospheres, we have established that if the source of vorticity is placed in the north instead of the south, the average of $T_{\theta\ r}$ over a cycle is negative, consistent with the transport of electromagnetic momentum southward across the equator. Data on the phase relations of the fluctuating signal observed at the northern period are given by *Provan et al.* [2011, Figure 11]; they find that ΔB_θ leads ΔB_r by $\sim$150°, implying that the product of the perturbations over a rotation period is negative, consistent with a source in the north. Data and simulation together provide support for the view that there are distinct sources of periodic momentum in the north and in the south and that the hemisphere in which the sources are located can be distinguished by the sign of the average over a cycle of $\Delta B_\theta \bullet \Delta B_r$ in the equatorial plane.

3.3. Azimuthal Currents

[25] Azimuthal currents are present throughout the equatorial plane, some widely distributed, some quite intense and localized either in radial distance and azimuthal extent. The simulated current density in the equatorial plane is illustrated at different rotation phases in Figure 5. Unit vectors representing the perturbation magnetic field can be seen to rotate between successive frames and thereby reveal the changing rotation phase. The colors (reds and yellows) indicate that the azimuthal current is positive everywhere. The global average ring current accounts for the highly stretched field structure of the outer magnetosphere and the disk-like geometry of the equatorial plasma sheet. More localized currents are referred to as azimuthal ring currents, and include a structure fixed in local time but varying periodically in intensity and a weaker

---

Figure 3. (a–d) Magnetic perturbation vectors in the equatorial plane. For each pair of images, the plot on the left is from the data analysis of *Andrews et al.* [2010], flipped so that the sun is to the left. The black arrows show rotation phase, with 0° (+integral multiples of 360°) defined as the phase at which the symmetry axis of the equatorial core field points toward noon. Color represents the sign of the B_θ perturbation, with red for positive (southward-pointing) values and blue for negative values. The plots on the right of each pair are from equivalent rotation phases of the simulation, with colors used as for the data plots. A reference vector showing 5 nT magnitude is included at the bottom left of each plot. Dashed circles are shown every 5 R_S.
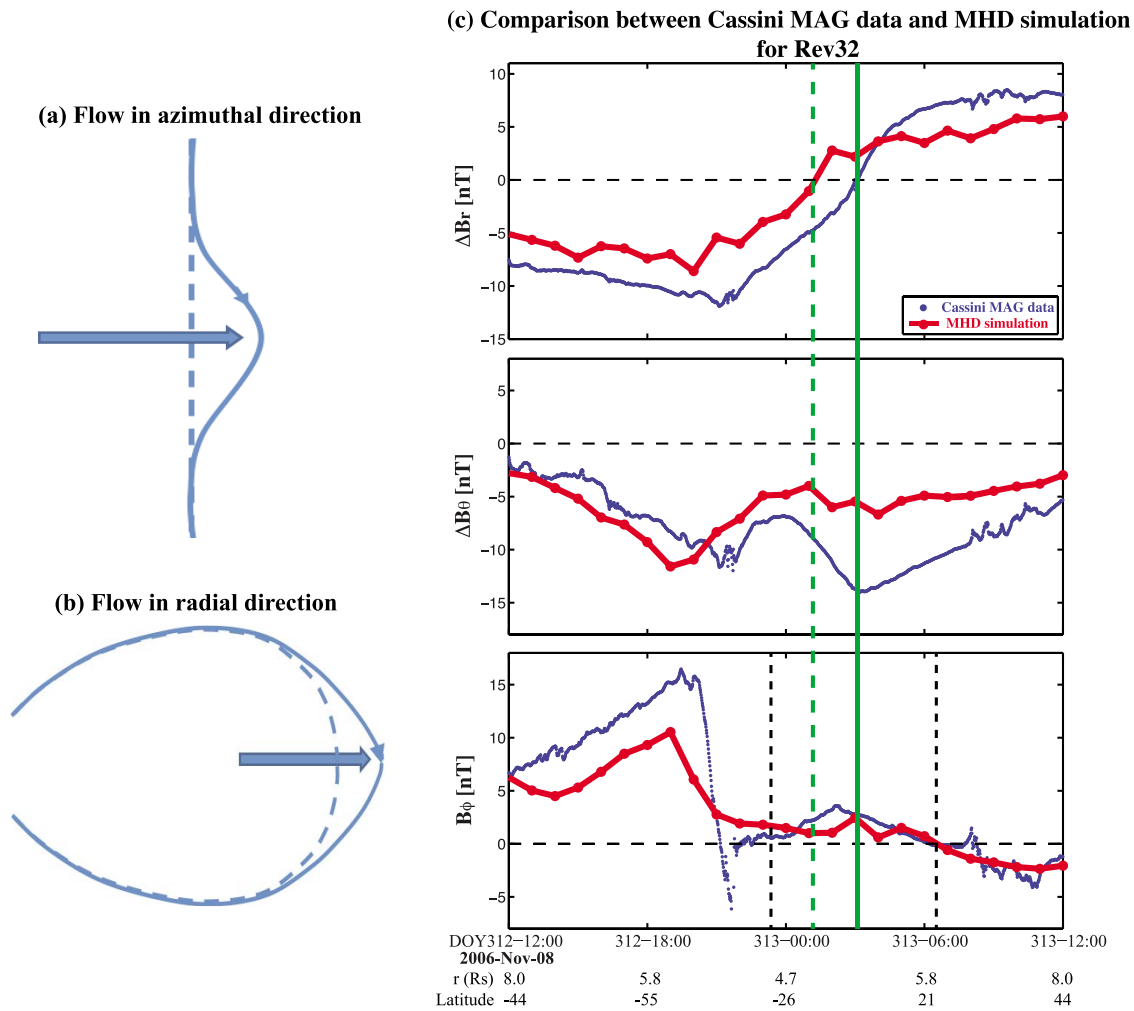
(a) Flow in azimuthal direction

(b) Flow in radial direction

(c) Comparison between Cassini MAG data and MHD simulation for Rev32

Figure 4. (a and b) Schematics of the distortion of a field line (originally the dashed line terminated at both ends in the ionosphere) by plasma flow in the vicinity of the equator. The flow stretches the field line, producing a bend around the flow vector (of the azimuthal field in Figure 4a and of the radial field in Figure 4b). In both cases, the perturbed component of the field reverses sign across the equator. (c) The perturbation field measured by Cassini on November 08–09, 2006 on an orbit that crossed the equator moving rapidly from south to north. The data are shown as blue solid curves and model results are plotted as red traces. The solid green vertical line marks the crossing of the magnetic equator in the data and the dashed green line identifies magnetic equator crossing in the model results. The dashed black vertical lines mark approximately the start and the end of half of the Doppler-shifted SKR cycle.

rotating structure whose intensity also varies periodically. The most intense azimuthal current is located in the night through morning sector and remains outside of 10 R_S. This localized current is analogous to the asymmetric ring current at the Earth, with largest amplitude in the post midnight sector instead of the pre-midnight sector observed at the Earth because of the reversal of the dipole orientation between the two systems. The rotating azimuthal ring current is evident between 12 and 15 R_S only at some rotation phases (at 200, 202:30, 210:00 and 212:30 but not at other time steps) and only in the afternoon sector. As the rotating asymmetric ring current encounters the fixed asymmetric ring current (e.g., at 205:00), the latter weakens in intensity, growing strong again only after a few hours have passed (e.g., at 210:00). The weakening of the rotating current

occurs concurrently with so many other changes of the system that it is unclear just what causes this response.

3.4. Mass Density Perturbations

[26] In Figure 6 we show the mass density at the time steps illustrated for the azimuthal current density in Figure 5. In Figure 6c at 205:00, weak density enhancements are present post midnight and in the afternoon sector. In Figure 6d, roughly a quarter of a cycle later at 207:30, a mass enhancement is evident near dusk without a counterpart on the morning side of the magnetosphere. By 210:00, there is a strong mass asymmetry (Figure 6e) with the highest mass localized pre-midnight. In the 5 h separating Figures 6c and 6e, the locus of the peak mass perturbation on the afternoon side has moved at a rate that cannot be distinguished from corotation. However, in the next 2.5 h (see Figures 6e
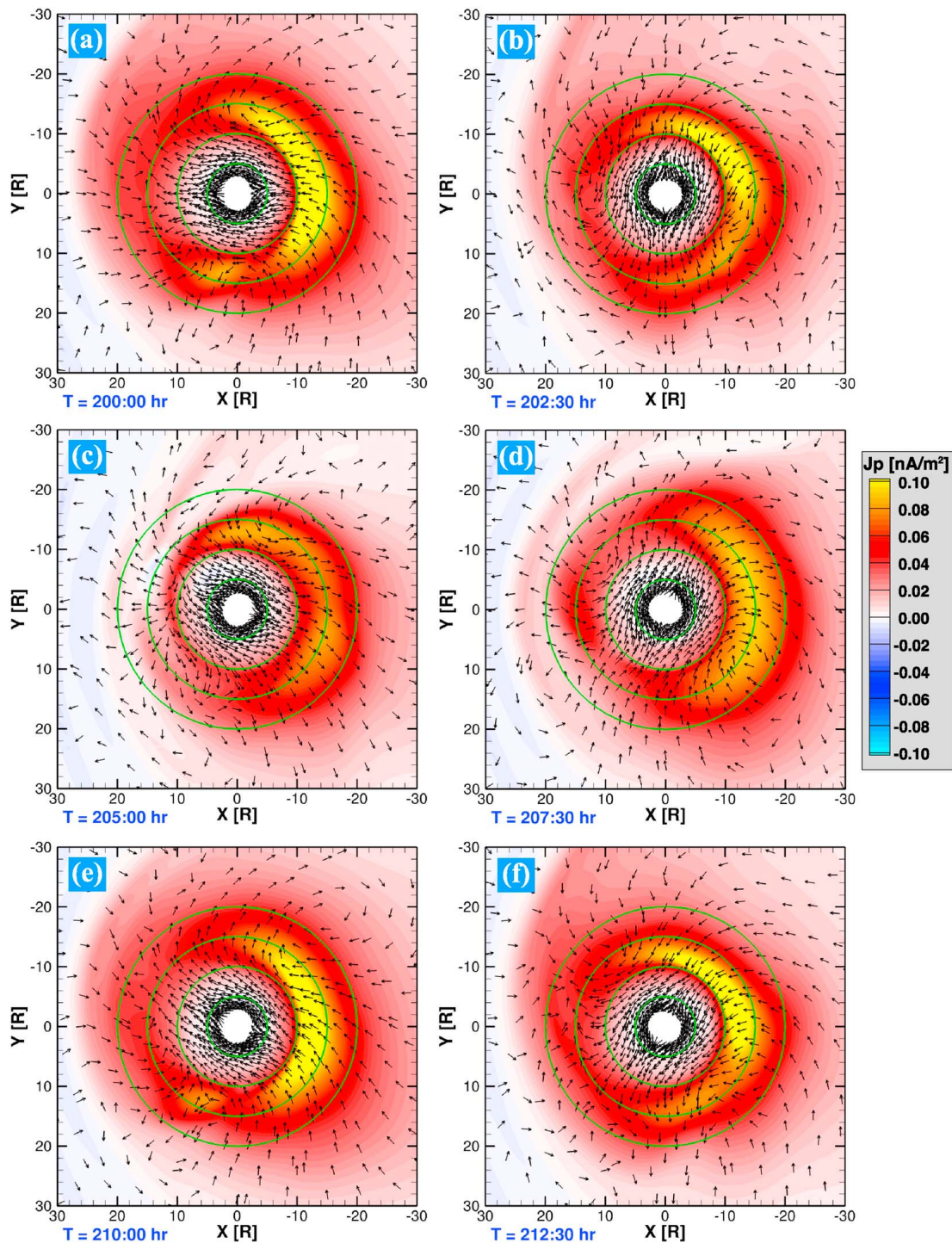
Figure 5. (a–f) Snapshots from the simulation. The azimuthal current density (J_P) is shown in color with black arrows that represent unit vectors along the perturbation magnetic field superimposed. Figure 5a is taken at hour 200:00, and the subsequent panels are successively 2:30 h later.

and 6f), the peak mass density rotates much more slowly. At 215:00 (not shown), a new mass density peak emerges in the afternoon sector. This temporal sequence recurs each cycle.

[27] *Gurnett et al.* [2007] have reported that the peak electron density between 3 and 5 R_S is organized by rotation phase. As their data were acquired only in the dusk sector (between roughly 13.5 and 01 LT), we compare them with

rotational variations measured at fixed points along the dusk meridian in Figure 7. As in the data, the simulated number density varies at the rotation period over a restricted range of radial distances, changing by roughly a factor of 2 between minimum and maximum. The L-shells on which the density variation appears is centered at ∼6 R_S. The mass density peak occurs at larger radial distance in the simulation than in
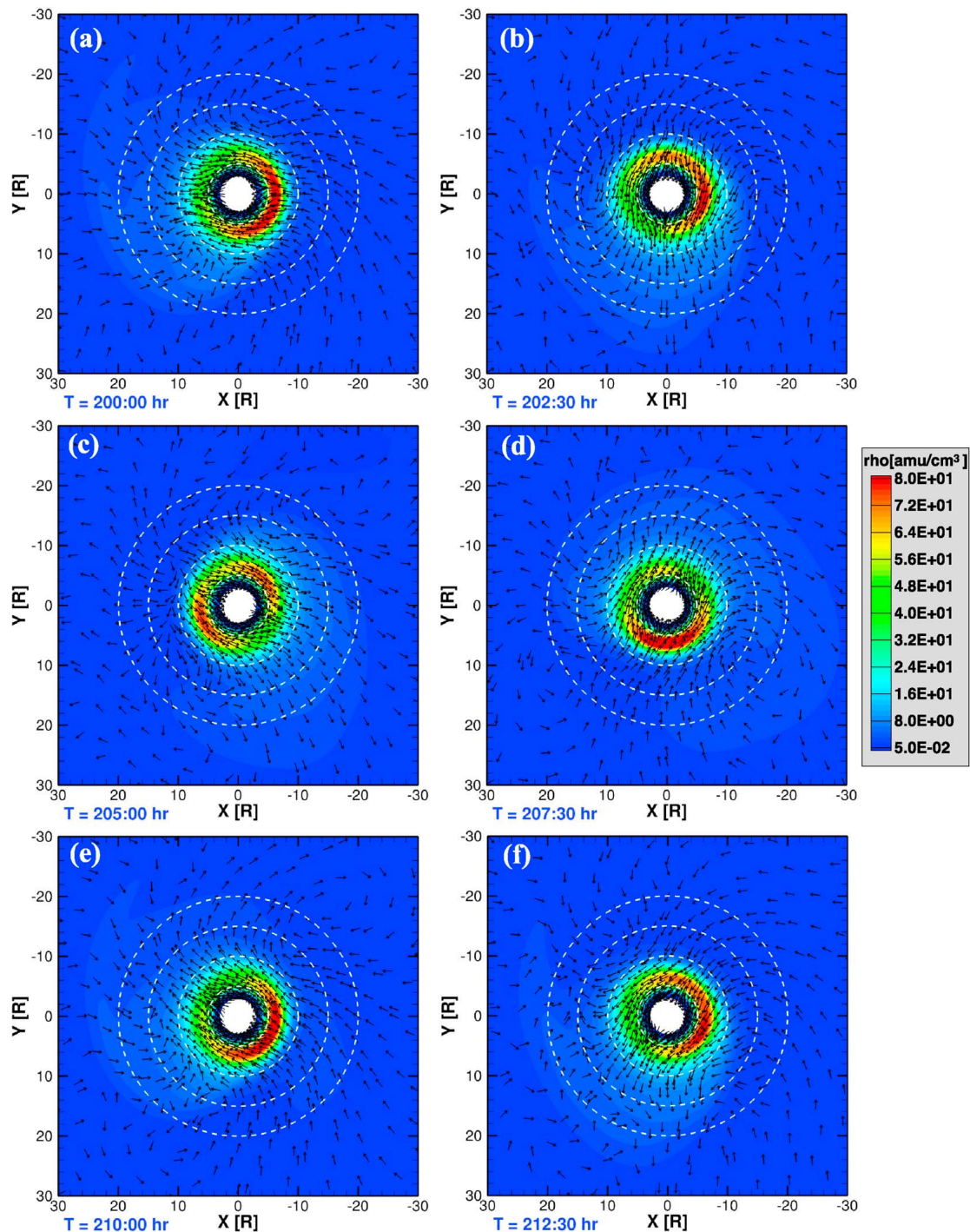
Figure 6. As for Figure 5 but for the mass density.

the data, probably because both the inner boundary and the mass loading peak (somewhat outward of the orbit of Enceladus [*Richardson et al.*, 1998; *Sittler et al.*, 2008]) have been shifted outward in the simulation. As described in Section 2, the inner boundary cannot be moved inside of 3 R_S without an unacceptable increase of computing time, nor can we model the regions inside of 4 R_S without invoking some additional constraints. The consequence is that anomalies in the inner magnetosphere may appear at somewhat larger radial distances in the model than in the data. In the vicinity of 6 R_S, B_ϕ varies between ~± 2 nT over a rotation period in both data and model. However, the peak of the modeled B_ϕ variation precedes the peak density by roughly 1/4 cycle, whereas in the data they are in phase. We have not been able to account for this discrepancy in phase, but suspect that it may relate to the assumption of uniform ionospheric conductance, which is inappropriate in the dusk sector at the time the data were acquired (midway between solstice and equinox).
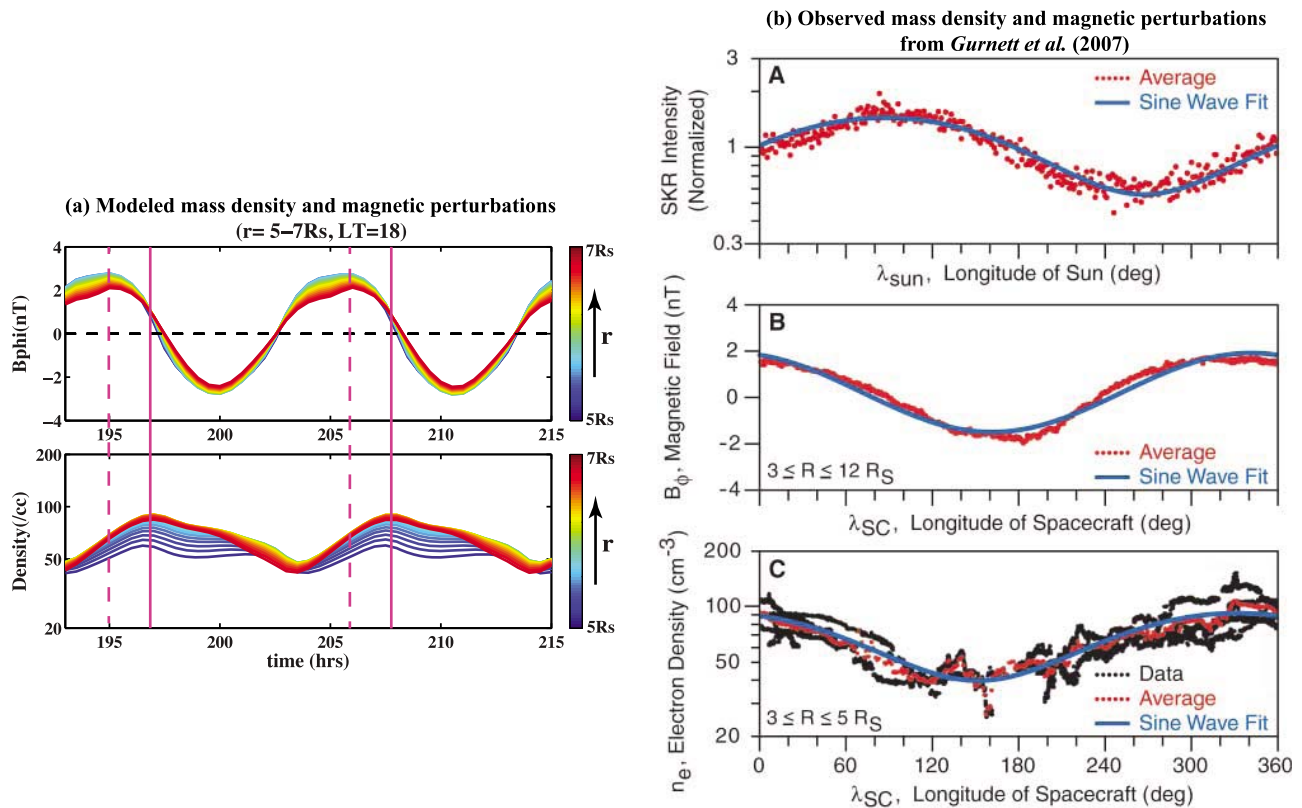
Figure 7. Samples of mass density and magnetic perturbations versus time: (a) from simulation at a range of radial distances on the dusk meridian between 5 and 7 R_S, (b) from *Gurnett et al.* [2007] sampled along spacecraft trajectories (orbits 3, 4, 5, 15 and 16) on the dusk side of the magnetosphere. Vertical lines in Figure 7a are separated by one rotation period.

3.5. Periodic Plasmoid Releases

[28] Thus far, we have discussed quasi-steady rotating responses to the ionospheric flows, but the magnetosphere also exhibits periodic magnetospheric convulsions associated with plasmoid releases (see, for example, the magnetospheric simulations of *Hansen et al.* [2000], *Fukazawa et al.* [2007], and *Zieger et al.* [2010]), tail flapping, and boundary oscillations. In Figure 8 we illustrate the dynamic response of the outer magnetosphere that is observed on each rotation. In Figure 8a, field lines that cross the equator at 20 R_S are shown at hour 198:00. By hour 200:00, the field lines on the night side begin to stretch (note the strong azimuthal current at this time step in Figure 5a). The stretching increases in subsequent time steps as a plasmoid forms (looped field lines at 203:00 that disconnect in subsequent time steps). Weak pressure enhancements appear in the vicinity of the looped field lines. The equatorial pressure peak on the night side weakens as the plasmoid goes down the tail and at the same time, the azimuthal current intensity decreases (see time 205:00 in Figure 5). By 207:00 the field configuration has returned to a quiescent configuration and the nightside pressure increases, with little subsequent change until renewed stretching begins at about 210:00.

[29] The dynamics of the interval illustrated repeat every rotation. It seems likely that the periodic plasmoid releases inject heated plasma into the inner magnetosphere. Such injections can account for the periodic intensification of

energetic neutral atom clouds observed by Cassini [*Paranicas et al.*, 2005; *Carbary et al.*, 2008; *Mitchell et al.*, 2009a]. It is of particular interest to note that in our simulation the plasmoid release occurs as the upward current from the south rotates into the morning sector [*Jackman et al.*, 2009], where the SKR emissions are most intense. Thus the processes in the inner magnetosphere linked to plasmoid release down the tail can explain the "recurrent ENA enhancements" that "coincide closely with bursts of Saturn kilometric radiation" [*Mitchell et al.*, 2009a].

[30] Plasmoids have been observed by Cassini in Saturn's magnetotail [e.g., *Jackman et al.*, 2007, 2008; *Hill et al.*, 2008]. However, a recent survey by *Jackman et al.* [2011] using the Cassini magnetometer data obtained during the deep tail orbits in 2006 identified only 34 plasmoid events. The number of plasmoids reported so far appears much smaller than what it would be if plasmoids are pinched off each rotation period as suggested by ENA observations and our model. However, most of the Cassini orbits from which data were used for plasmoid survey are equatorial orbits, which are not optimal for directly detecting plasmoids because the magnetospheric current sheet during the time between solstice and equinox is distorted by the oblique solar wind flow such that it is displaced away from the equator [*Arridge et al.*, 2008a]. Furthermore, our model and the local time distribution of newly formed ENAs [*Mitchell et al.*, 2009a, 2009b] indicate that plasmoids tend to form in the post midnight sector, where Cassini in situ
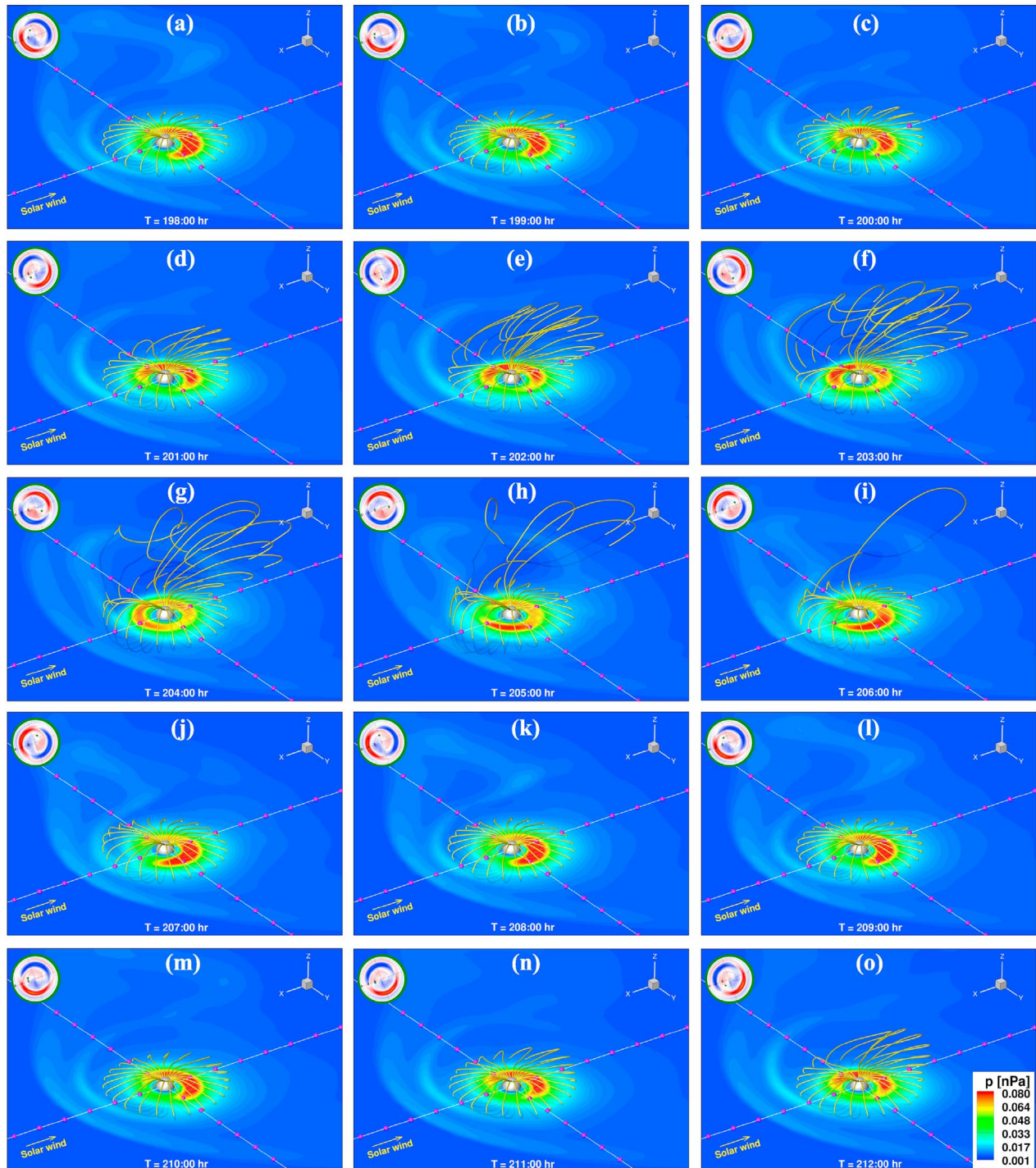
Figure 8. (a–o) A three-dimensional view of field lines (yellow) that cross the equator at 20 R_S at every hour of local time. Pink balls mark off every 10 R_S along the axes. The coordinate system has X pointing toward the Sun and Z along Saturn's spin axis. Images are taken every hour between 198 h and 212 h (which includes the interval illustrated in Figures 4 and 5). Color represents thermal pressure. Shadowed curves follow the portions of field lines that lie below the equatorial plane as, for example, for the looped field line in the tail in Figure 8i (hour 206). The insert in the upper left of each panel is a view from the north of field-aligned currents into and out of the southern ionosphere, with colors as shown in Figure 2. In the inserts, noon is to the left, dawn to the top.
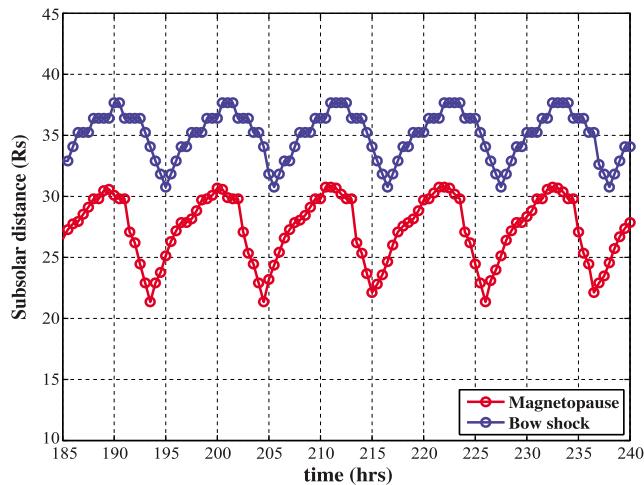
Figure 9. The subsolar locations of the bow shock and the magnetopause extracted from the simulation as function of time. The two boundaries oscillate at the planetary rotation period, consistent with Cassini observations of *Clarke et al.* [2010a, 2010b]. Comparison with Figure 7 shows that the minimum corresponds to the time of plasmoid release.

measurements are relatively sparse. Therefore, the probability of plasmoid occurrence needs to be further evaluated taking into account the location of the spacecraft relative to the tail current sheet and the amount of time the spacecraft spent in different local time sectors.

3.6. Periodic Boundary Oscillations

[31] The boundaries of the magnetosphere also respond to the periodic releases. Relatively abrupt pressure changes occur at the bow shock and at the magnetopause. From Figure 8, it can be seen that both boundaries move to larger distances from the planet during the relatively quiet part of the cycle shown (e.g., hours 207–210 in Figure 8) and move inward but begins to move inward again as the plasmoid begins to break off and move toward positive Z and down tail (e.g., 211–212 in Figure 8), reaching a minimum roughly when the plasmoid is largest (e.g., 204–205 in Figure 8). Figure 9 shows the subsolar locations of the bow shock and the magnetopause over multiple cycles, plotted as a function of time. The two boundaries oscillate at the planetary rotation period, consistent with Cassini observations of *Clarke et al.* [2010a, 2010b]. However, the form of the oscillations is very non-sinusoidal, not at all like what one might expect from relatively small amplitude Kelvin-Helmholtz oscillations of the boundary [e.g., *Masters et al.*, 2010]. The amplitude reported by *Clarke et al.* [2010a, 2010b] has a typical value of ∼2 R_S and occasionally reaches 4–5 R_S. If one fits the modeled boundary oscillations with a sine wave, the amplitude of the sine fit is about 2 R_S, consistent with the Clarke et al. results.

3.7. Current Sheet Flapping

[32] The formation and release of the plasmoids is also associated with north-south displacements of the current sheet. Figure 10 shows the location of the magnetotail current sheet as a function of downtail distance at various phases of rotation. In Figure 10a, those positions are shown

for a run in which the solar wind elevation angle was set to 15°, corresponding to solar wind flow at 105° to the spin axis. Figure 10b [from *Khurana et al.*, 2009], shows the locations of current sheet crossings (green points) from in situ data. The latitudes observed in the data have been rescaled to the maximum possible solar wind elevation angle (26.73°) by multiplying a factor $f = 26.73/$latitude (degrees). In Figure 10c, we have applied the same rescaling to the results of Figure 10a. In Figure 10d, our results are plotted on top of the data plot. To within the variations allowed by non-radial solar wind flows, the simulation corresponds to the observations. The flapping in this model does not arise from anomalous plasma density during half of each rotation cycle as suggested by *Khurana et al.* [2009].

3.8. Comparison With Measured Magnetic Field Along Cassini Orbits

[33] To this point in the paper, we have compared simulated results with spacecraft data averaged over multiple orbits. One should not anticipate detailed representation of the data on individual orbits for several reasons. The data are not acquired in a magnetosphere subject to a steady non-reconnecting solar wind, which is the situation modeled. In averaged data sets, the stochastic response of the magnetosphere to solar wind-driven changes is suppressed, whereas the data on individual passes reflect specifics of the external conditions. Also, as noted above, the model does not account for the tilt of the dipole moment appropriate to most Cassini orbits. This means that for early parts of the missions when the current sheet was tilted by 15° or more relative to the XY–KSM plane, crossings of the current sheet in the tail will be displaced in time from the corresponding crossings in the model. Furthermore, the modeled inner boundary at 3 R_S produces anomalous effects on data taken at small radial distances near closest approach. Nonetheless, we find that on most passes the simulation reproduces many critical features of the measurements made along individual orbits.

[34] In Figure 11 we show the three components of the magnetic field measured along representative orbits of two different types. Figure 11a shows data from a highly inclined orbit in November 2006 with inserts showing the projection of the orbit onto the XZ and XY planes of the KSM coordinate system. All components of the measured and simulated traces oscillate at the Doppler-shifted period of planetary rotation. (The Doppler shift corrects for spacecraft motion relative to the rotating planet and is particularly important near periapsis for equatorial orbits [*Cowley et al.*, 2006; *Arridge et al.*, 2011].)

[35] Overall the pairs of traces are similar in structure. A few clear discrepancies are readily accounted for. For example, the data in Figure 11a were acquired in November 2006 at a time when the inner portion of the current sheet was tilted nearly 15° with respect to the XY plane whereas the simulation does not allow for a tilt. The difference of the tilt explains why the current sheet crossings occur at different times in the two sets of traces. The data start near midnight, with the spacecraft moving southward and sunward. The modeled current sheet ($Z = 0$) crossing occurred just before the beginning of 11/05, where dB_r and dB_ϕ changed sign whereas the physical current sheet, indicated by sign changes of the measured dB_r and dB_ϕ, was not encountered until early on the next day. Thus the dominant cause of the
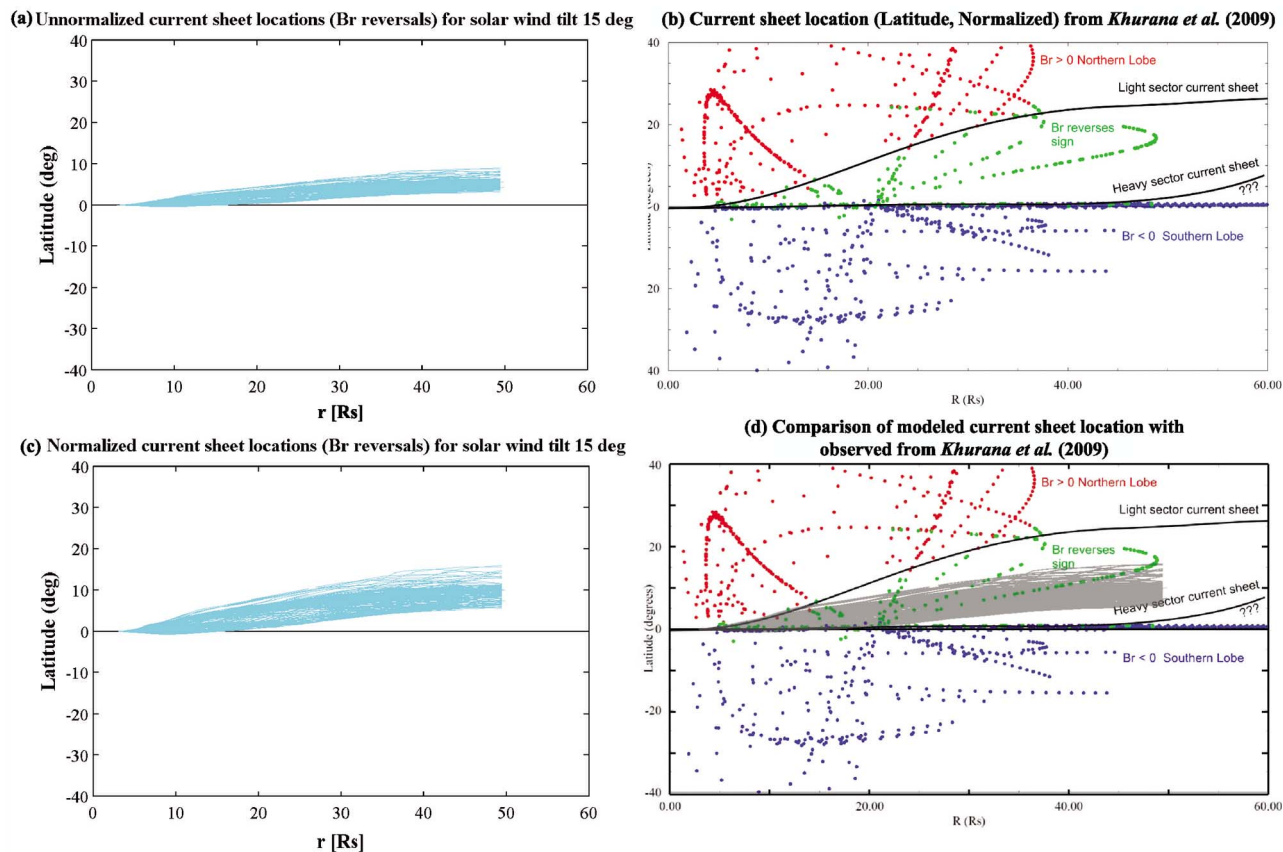
Figure 10. (a) Locations of the magnetotail current sheet at different phases of ionospheric rotation from a simulation with 15° solar elevation angle. (b) From *Khurana et al.* [2009], locations of encounters with Saturn's magnetotail current sheet plotted as latitude versus distance. B_r is taken as a proxy for the location of the spacecraft. The data have been rescaled by multiplying the observed latitude by a factor $f = 26.73$/latitude (degrees) to represent latitudes that would be observed at maximum solar wind elevation angle (26.73°). Points are plotted every hour and are red if B_r remains positive, blue if B_r remains negative, and green if both signs are observed. The latter is taken as evidence of a location close to the current sheet center. (c) As in Figure 10a but with the latitude rescaled as in the *Khurana et al.* [2009] figure. (d) Rescaled locations of the current sheet in the simulation (in gray) superimposed on the *Khurana et al.* [2009] figure.

inaccuracy of the model on 11/05 reflects the use of an inappropriate solar wind attack angle.

[36] In Figure 11a, another interval in which the pairs of traces differ occurs near closest approach and again can be attributed to known deficiencies of the model. The dips in dB_θ are far smaller in the model than in the data. This we attribute to the way in which the inner boundary is handled in the model. For this orbit closest approach is at 4.7 R$_S$, close enough to the inner boundary that its effects smooth out variations driven from larger radial distances.

[37] Despite evident defects of the model results, it is generally successful in representing the data. The amplitude and phase of the periodic variations are captured reasonably well (for intervals in which the model places the spacecraft on the proper side of the current sheet) and the times of the periodic depressions in dB_θ related to the asymmetric ring current are appropriate. A very abrupt variation of B_ϕ occurs on Nov. Eight near 21:00 UT in both model and data. This strong field rotation is associated with the field-aligned current linking southern and northern ionospheres, although

grid resolution and low sampling rate reduce the amplitude of the jump in the model.

[38] In Figure 11b, model and data for an equatorial orbit (shown in the inset) are compared. The oscillations of model and data are in phase and with amplitudes that are generally similar. Where the amplitudes differ substantially (such as on days 4/24 and 4/25 for dB_r and B_ϕ), the difference, once again, can be attributed to the failure of the model to include the oblique flow of the solar wind or to the influence (for dB_θ on days 4/28 and 4/29) of the bloated inner boundary in the simulation.

3.9. Rotation Phase Control of the Intensity of Field-Aligned Currents Flowing Out of the Southern Ionosphere

[39] The FACs in the ionosphere are, in part, directly driven by the vortical flows imposed in the southern ionosphere and, in part, imposed by flows and pressure gradients in the magnetosphere. The former source produces a FAC system fixed in the rotating frame. The latter sources
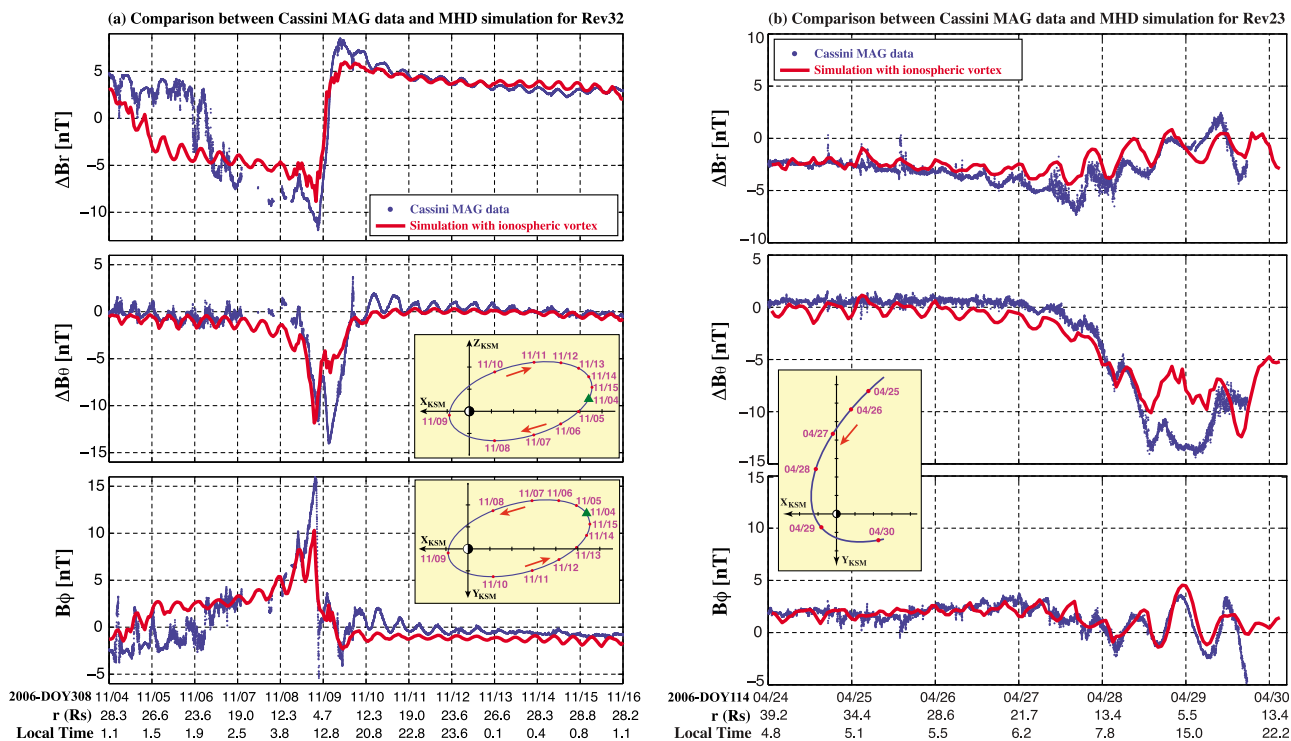
Figure 11. Three components of measured and modeled field from which the contribution of an internal dipole moment have been subtracted. Data and simulation are shown for (a) an oblique pass in November 2006, with insets showing the orbit in the *xz*-plane and the *xy*-plane, and (b) for an equatorial pass in April 2006, with inset showing the orbit in the *xy*-plane. Data are plotted in blue and the simulated results are plotted in red.

introduce local time asymmetries into the ionospheric current system, and those asymmetries can account for the local time variation of the intensity of SKR emissions. *Lamy et al.* [2009] found just such behavior in the SKR emissions, i.e.,

emissions from a rotating source that intensifies as it rotates into the morning sector.

[40] Where upward current becomes sufficiently intense, field-aligned electric fields commonly develop to accelerate
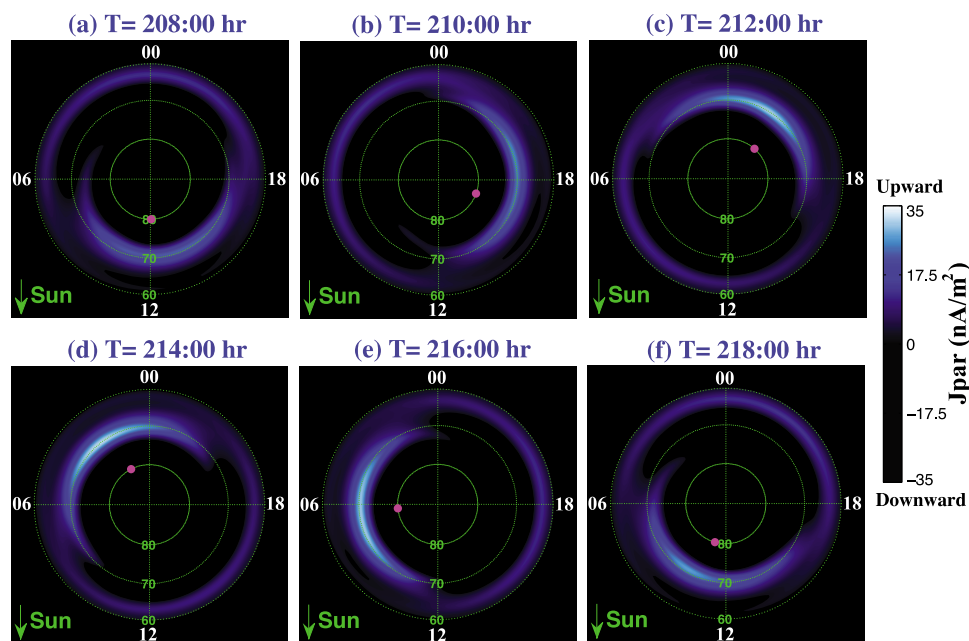

Figure 12. (a–f) Upward current density from the southern hemisphere at different rotation phases in the simulation. The small pink circle shows the meridian of the center of the vortex driving upward current.
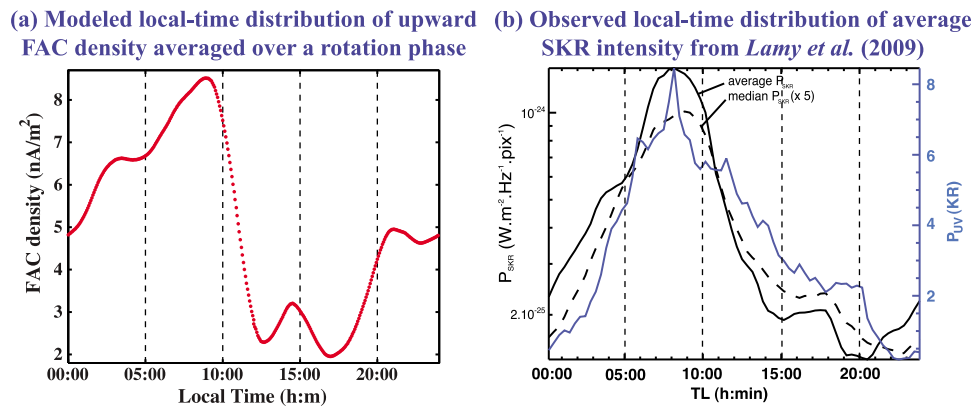
(a) Modeled local-time distribution of upward FAC density averaged over a rotation phase

(b) Observed local-time distribution of average SKR intensity from *Lamy et al.* (2009)

Figure 13. (a) Average over a rotation phase of upward field-aligned current from the southern ionosphere versus local time (LT) from the simulation. (b) UV power (blue) and SKR intensity (black) versus LT adapted from *Lamy et al.* [2009]. Dashed curve is the median SKR intensity.

the current-carrying electrons. Accelerated electrons, in turn, generate the SKR emissions [*Wu and Lee*, 1979; *Galopeau et al.*, 1989], so it is reasonable to identify the intense upward current as the source of SKR. In Figure 12 we show the modeled intensity of FACs upward from the southern ionosphere versus local time at different rotation phases. By following the location of the pink circle at the meridian of the vortex center, one can follow the rotation of the current driven by the imposed vortex. Evident from the figure is that the peak upward current rotates at the imposed period, but that the peak intensity is not constant. Following the pattern through a cycle, one sees that the current is weakest near dusk and reaches maximum intensity in the morning sector.

[41] In Figure 13a, we plot the intensity of the modeled current versus local time averaged over a complete rotation. We also reproduce a figure from *Lamy et al.* [2009, Figure 5] (Figure 13b) showing the average of the observed SKR intensity versus local time of the source over many rotation periods. The variation with local time of the modeled FAC intensities is similar in the two plots. The localization of the peak intensity between 06:00 and 10:00 LT matches the localized peak of the observed intensity variations of SKR, consistent with an expectation that the rotating FACs drive the most intense SKR emissions as they rotate into the morning sector where the rotating currents are supplemented by magnetospheric currents fixed in local time [*Southwood and Kivelson*, 2009].

4. Comparison With Other Models

[42] Numerous models have been suggested for the source of the electromagnetic periodicities observed in Saturn's magnetosphere. An excellent summary is provided by *Mitchell et al.* (2009b). Recently attention has focused on various rotating anomalies. They include (a) a magnetospheric convection-driven plasma flow in the inner magnetosphere [*Gurnett et al.*, 2007; *Goldreich and Farmer*, 2007], (b) recurrent reconnection and plasmoid release [*Mitchell et al.*, 2009a], (c) a rotating plasma pressure or density anomaly [*Carbary et al.*, 2007b; *Khurana et al.*, 2009] and a closely associated rotating partial ring current model [*Brandt et al.*, 2010], (d) a plasma cam [*Burch et al.*,

2009], and (e) a rotating system of field-aligned currents linking the northern and southern ionospheres [*Southwood and Kivelson*, 2007].

[43] The models listed account for the data that they were designed to explain, but are limited in predictive ability. Models (a)–(d) drive the periodicity from sources at or near the magnetospheric equator. Consequently they should produce field perturbations that are antisymmetric about the equator (as illustrated in Figure 4). For example, the effect of flows such as those called for in (a) and the imposition of a cam-like perturbation such as that called for in (d) should bend field lines at or near the equator. The effect should be evident in data on highly inclined orbits as relatively abrupt 180° changes of the oscillation phase of the transverse components of the perturbed field as the spacecraft crosses the equator, but the data do not reveal such changes (Figure 4 and discussion thereof). Additional questions relate to how such models can be extended to explain different periods linked to northern and southern hemisphere SKR emissions.

[44] Model (c) calls for the development of a density or pressure structure embedded within the rotating near-equatorial plasma. In order for models of this type to impose signals at the SKR period, either they must be embedded in plasma rotating at the SKR period or they need to arise from some rotating source that creates a disturbance propagating through the plasma rest frame. Full corotation is ruled out by evidence that the plasma in most parts of the equatorial plane rotates only at 50% to 70% of full corotation [*Thomsen et al.*, 2010]. (In the simulation, we find the average plasma flow near the equator in the inner magnetosphere is at ∼80% of corotation and periodic fluctuations are of order 10%.) The alternative that the rotating structure is imposed as a propagating structure raises the as-yet-unanswered question of what imposes the disturbance and what causes it to propagate relative to the plasma rest frame.

[45] Model (b) does not require full corotation, but assumes that a recurrent reconnection in the tail will resume at the same rotation phase independent of changes of magnetospheric conditions imposed by the changing solar wind and particularly associated with shocks and IMF rotations [*Jackman et al.*, 2005; *Zarka et al.*, 2007; *Zieger et al.*,

2010]. Although the dynamics of the magnetosphere is thought to be dominated by internal processes, the solar wind does impose changes of scale, and the internal dynamics are known to respond. For example, Hubble observations have linked significant changes of auroral emissions to the effect of solar wind compression [*Clarke et al.*, 2005] and it is well established that the magnetospheric scale size can vary by large factors [*Arridge et al.*, 2006; *Achilleos et al.*, 2008]. Compression and expansion affect the density and angular velocity of the plasma, and it is unclear how the rotation phase of periodic plasmoid release can be unaffected by intermittent large scale dynamics of the system.

[46] Model (e) is successful in accounting for the rotating magnetic perturbations seen near the equatorial plane that motivated its development. The field-aligned currents described were later observed in the data of non-equatorial orbits [*Southwood and Kivelson*, 2009]. However, while accounting for the magnetic perturbations observed, the model does not explain other periodicities in the system nor does it give any insight into how the current system might arise.

5. Discussion and Summary

[47] Identifying the source of the electromagnetic periodicity at Saturn has presented a challenge since modulation of SKR power at a period near 10.7 h was first discovered in the 1980s. In this paper we have investigated a model that attributes the periodicity to vortical flow rotating at the rate of the upper atmosphere. The focus on the upper atmosphere/thermosphere arises from a desire to account for the very slow rate of change of both the period and the phase of the peak SKR emissions. The interior of Saturn can be ruled out as the location of the source because its rotation period cannot change on the observed time scale of years. The magnetosphere itself could respond to the Enceladus mass input with plasma releases at a natural period (see, for example, estimates of pertinent time scales for Jupiter by *Vasyliūnas* [1994]), thereby providing a driver for electromagnetic periodicities. However, we do not believe that the phase of the plasma releases can be maintained in a magnetosphere that experiences intermittent major compressions and expansions imposed by extreme pressure variations that are typical of the solar wind at Saturn's 10 AU orbit [*Jackman et al.*, 2005]. Changes in scale of the magnetosphere under changing solar wind dynamic pressure, and associated changes in plasma rotation velocity, should produce phase jumps in the modulation of SKR even if a preferred periodicity were to recur as the system relaxed back to its average configuration. Yet persistent jumps in phase are not observed. (*Arridge et al.* [2011] find "little evidence" supporting the proposed clock reset proposed by *Carbary et al.* [2007c].)

[48] As contrasted with the interior, the upper atmosphere/thermosphere is a region in which the rotation rate could plausibly change at a rate as large as 1% per year and yet, as contrasted with the magnetosphere, large variations of solar wind pressure would not discontinuously change the phase of embedded structures. This region also should be sensitive to changes of solar illumination, thus accounting for the slow variation of SKR periods [*Gurnett et al.*, 2009a, 2009b, 2010; *Mitchell et al.*, 2009a; *Southwood and Kivelson*, 2009;

Smith, 2011]. Thus we argue that an azimuthal asymmetry of the winds of the upper atmosphere, something like a thermospheric "red spot," carried around the spin axis at a very slowly varying rotation rate by the upper atmosphere, may be the source of the perturbations observed in the magnetosphere. Unfortunately, the upper atmosphere and the thermosphere cannot be imaged as is the troposphere [e.g., *Sánchez-Lavega et al.*, 2004, 2007], so neither wind speeds nor patterns are known. Thus we are forced to speculate on their structures and flow speeds, and here we have used the indirect evidence of magnetospheric and ionospheric properties to propose aspects of thermosphere/ionosphere winds and flows.

[49] The upper atmosphere/thermosphere is coupled through collisions to the ionosphere. The ionosphere, in steady state, rotates at the rate of the magnetospheric regions to which it is magnetically linked; at Saturn the period of that rotation is longer than the SKR period. Thus, in order to drive magnetospheric responses at the SKR period, the perturbations imposed from the upper atmosphere must propagate azimuthally in the ionosphere's rest frame in the sense of planetary rotation. One can picture the atmospheric perturbation setting up an ionospheric response in the way a candle flame moved beneath a metal plate produces a propagating hot spot on the plate.

[50] The form of flow perturbations imposed on the ionosphere must be capable of setting up field-aligned currents that couple the ionosphere to the magnetosphere, and for this reason we model the traveling disturbances as flow vortices. We place the center of the vortex at 70° latitude, in the region where the FACs of the cam current system have been identified and we impose an $m = 1$ azimuthal symmetry to accord with observations. For mathematical convenience, in the run on which we report in this paper, we introduced a pair of ionospheric vortices (see Figure 2). In order to assure ourselves that the results are largely independent of the specific form of the vortices, we have tested the sensitivity of the results in a short run using only one vortex, the one that drives upward FACs (red in Figure 2a). Results of this run are shown in Figures 14 and 15. From Figure 14 one sees that the structure of the ionospheric FACs differs little whether one drives the disturbances with a double vortex (Figures 14a and 14b) or a single vortex (Figures 14c and 14d), but the currents are weaker when the system is driven with only one of the two vortices. The reduction in the magnitude of the current is expected because the net energy input is lower in the single vortex case. In Figure 15 we show the equatorial responses as mass density distribution and azimuthal current density distribution at the same time step in the simulation for the dual vortex run (above) and the single vortex run (below). The general structure of these quantities and of the magnetic perturbations that are also plotted changes little when only a single vortex is imposed in the southern ionosphere. Thus it is likely that the results are not sensitive to the details of the structure imposed provided it is localized at an appropriate latitude.

[51] If, as in our model, the source of the periodicity is located in the upper atmosphere, the field perturbations will vary smoothly across the equator without change of phase and, consequently can be consistent with observations such as those shown in Figure 4. If the magnetosphere changes size in response to changes in solar wind dynamic pressure,
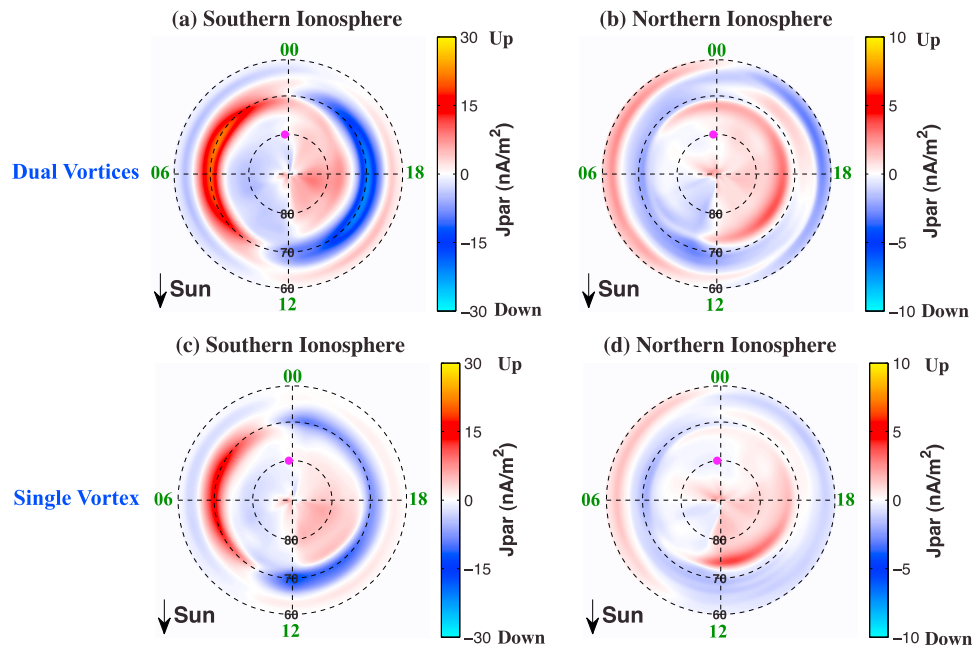
Figure 14. Comparison of field-aligned current density in the ionosphere arising from (a, b) a dual vortex in the southern ionosphere, as in Figure 2a, and (c, d) a single vortex in the southern ionosphere (only the one driving upward field-aligned current in Figure 2a). Model results are extracted from the time step T = 183:30 h.

both the magnetospheric and ionospheric rotation rates are expected to change, but the upper atmosphere is not expected to slow noticeably. Once the magnetosphere relaxes back to a characteristic scale size, the upper atmosphere will again impose perturbations on the ionosphere at the rotation phase present prior to the expansion or compression.

[52] Our model requires that a long-lived vortex be present in the upper atmosphere and the thermosphere to which it is coupled and that the momentum coupling between the upper atmosphere and the ionosphere be significant on a time scale of order the rotation period or shorter. Whether such requirements can be achieved through reasonable physical processes in the upper atmosphere and the ionosphere needs to be investigated further. However, it is worth noting that the type of vortical structure that we invoke is similar to that previously investigated as a thermospheric phenomenon by *Smith* [2006, 2011]. However, in order to obtain perturbations of the magnitude observed, we have invoked far faster flows than those he obtained from his analysis of the thermospheric response to a localized rotating heat source.

[53] Our MHD simulation gives generally good agreement with so many aspects of the periodicities observed at Saturn that we are encouraged to develop the model further and, in particular, to incorporate some aspects of the system that were not represented in the initial run. In future runs, we intend to set the angle between the solar wind and the spin axis to a value typical of the early part of the Cassini mission in order to model the warped plasma sheet and other north-south asymmetries in the system. We shall also allow the solar wind to vary in a manner representative of its typical behavior at 10 AU, including features such as shocks (forward and reverse) and field rotations in order to examine how the periodicity is affected by the associated

disturbances and how long it takes to recover from significant changes. We will also carry out runs in which we start with the periodically modulated magnetosphere that we have presented here and remove the driver in order to test whether the periodicity can be maintained simply from the persistence of the flow patterns and the periodic plasmoid releases.

[54] In other runs, we intend to impose flow vortices in both the southern and the northern ionospheres in order to investigate possible sources of dual frequencies. Because flux tubes must move as a whole, we will place the second vortex system on L-shells different from those that drive the perturbations at the southern period. This will allow us to assume a 10.6 h rotation period on the northern structures, implying zonal winds of order 60 m/s faster than those in which the southern vortex is located. Such latitudinal differences of wind speed are in the range observed in the troposphere [*Sánchez-Lavega et al.*, 2004, 2007]. Placing the northern vortex at a latitude somewhat >70° would be consistent with observations of the latitude of the northern source of SKR reported by *Cecconi et al.* [2009] and will allow, for example, the oscillations on open field lines to differ in the two hemispheres [*Southwood*, 2011], but will impose both frequencies on closed flux tubes, thus producing the "jitter" discussed by *Provan et al.* [2011].

[55] Although the dominant purpose of this paper is to present a coherent picture of the periodicities observed in Saturn's magnetosphere, it is of interest to point out that there is intriguing evidence that at Jupiter, too, there are magnetospheric phenomena that are modulated at a period a few percent longer than the period of rotation. The observations have been ascribed to a "System IV" periodicity (*Sandel and Dessler* [1988] and a review by *Thomas et al.*,
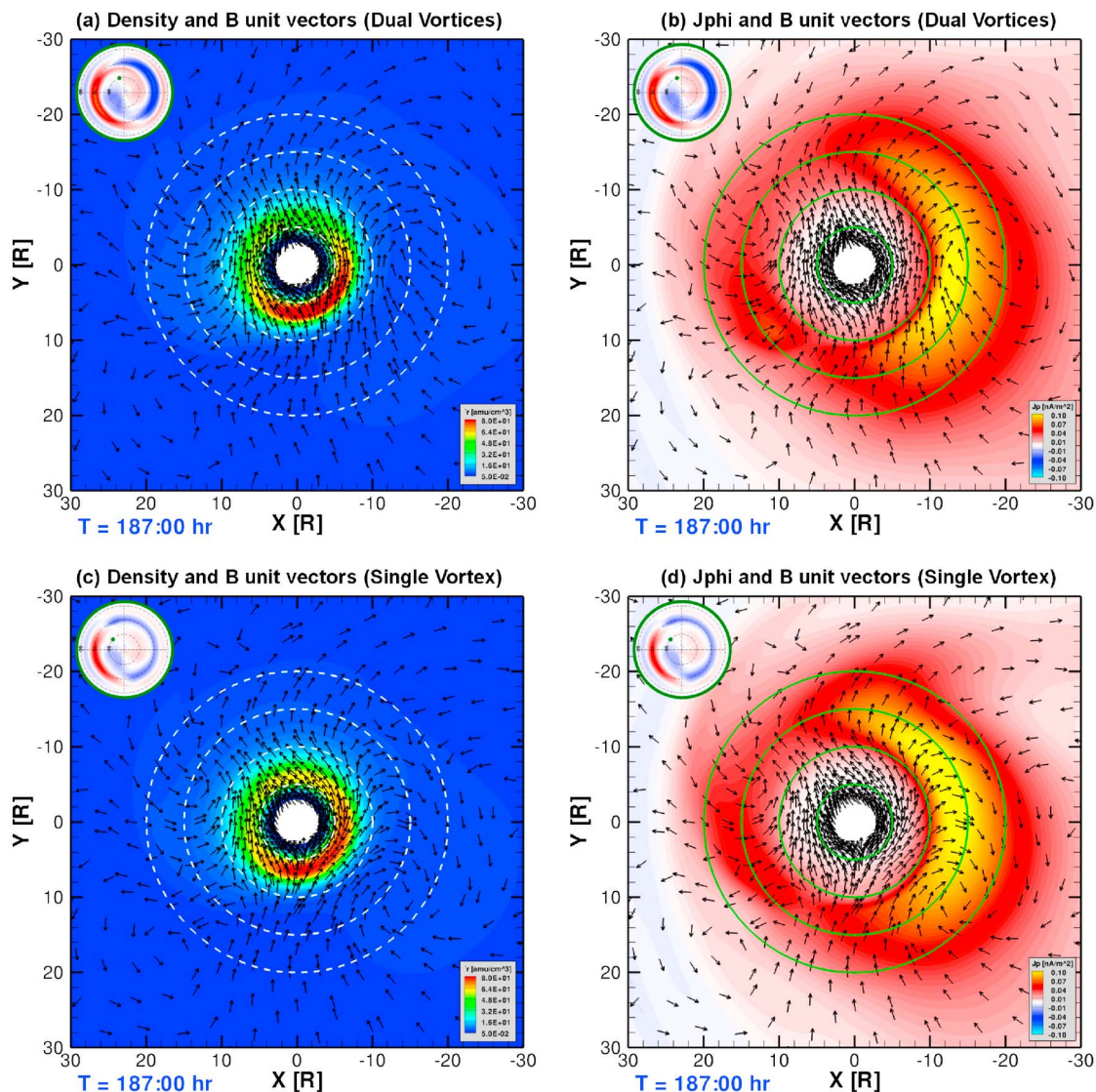
Figure 15. Comparison of magnetospheric responses from the simulation for (left) the mass distribution and (right) the azimuthal current distribution (a, b) using dual vortices in the southern ionosphere and (c, d) the simulation using only a single vortex. Black arrows are unit vectors representing the transverse magnetic perturbations.

[2004]). At Jupiter, the dominance of the periodicities linked to rotation has made it difficult to characterize the features of the system that vary at this secondary periodicity. It is, however, possible that Jupiter, like Saturn, harbors flow anomalies rotating more slowly than the interior and that these anomalies impose periodicities on its ionosphere and magnetosphere. Once we feel confident that we understand the source of Saturn's periodicities, we may find application of our improved understanding to other magnetospheres of the solar system.

References

Achilleos, N., C. S. Arridge, C. Bertucci, C. M. Jackman, M. K. Dougherty, K. K. Khurana, and C. T. Russell (2008), Large-scale dynamics of Saturn's magnetopause: Observations by Cassini, *J. Geophys. Res.*, 113, A11209, doi:10.1029/2008JA013265.

Andrews, D. J., E. J. Bunce, S. W. H. Cowley, M. K. Dougherty, G. Provan, and D. J. Southwood (2008), Planetary period oscillations in Saturn's magnetosphere: Phase relation of equatorial magnetic field oscillations and Saturn kilometric radiation modulation, *J. Geophys. Res.*, 113, A09205, doi:10.1029/2007JA012937.

Andrews, D. J., S. W. H. Cowley, M. K. Dougherty, and G. Provan (2010), Magnetic field oscillations near the planetary period in Saturn's equatorial magnetosphere: Variation of amplitude and phase with radial distance and local time, *J. Geophys. Res.*, 115, A04212, doi:10.1029/2009JA014729.

Arridge, C. S., N. Achilleos, M. K. Dougherty, K. K. Khurana, and C. T. Russell (2006), Modeling the size and shape of Saturn's magnetopause

with variable dynamic pressure, *J. Geophys. Res.*, *111*, A11227, doi:10.1029/2005JA011574.

Arridge, C. S., K. K. Khurana, C. T. Russell, D. J. Southwood, N. Achilleos, M. K. Dougherty, A. J. Coates, and H. K. Leinweber (2008a), Warping of Saturn's magnetospheric and magnetotail current sheets, *J. Geophys. Res.*, *113*, A08217, doi:10.1029/2007JA012963.

Arridge, C. S., N. Andre, N. Achilleos, K. K. Khurana, C. L. Bertucci, L. K. Gilbert, G. R. Lewis, A. J. Coates, and M. K. Dougherty (2008b), Thermal electron periodicities at 20R$_S$ in Saturn's magnetosphere, *Geophys. Res. Lett.*, *35*, L15107, doi:10.1029/2008GL034132.

Arridge, C. S., et al. (2011), Periodic motion of Saturn's nightside plasma sheet, *J. Geophys. Res.*, *116*, A11205, doi:10.1029/2011JA016827.

Atreya, S. K., T. M. Donahue, A. F. Nagy, J. H. Waite Jr., and J. C. McConnell (1984), Theory, measurements, and models of the upper atmosphere and ionosphere of Saturn, in *Saturn*, edited by T. Gehrels and M. S. Matthews, pp. 239–277, Univ. of Ariz. Press, Tucson.

Brandt, P. C., K. K. Khurana, D. G. Mitchell, N. Sergis, K. Dialynas, J. F. Carbary, E. C. Roelof, C. P. Paranicas, S. M. Krimigis, and B. H. Mauk (2010), Saturn's periodic magnetic field perturbations caused by a rotating partial ring current, *Geophys. Res. Lett.*, *37*, L22103, doi:10.1029/2010GL045285.

Bunce, E. J., S. W. H. Cowley, and J. A. Wild (2003), Azimuthal magnetic fields in Saturn's magnetosphere: Effects associated with plasma sub-corotation and the magnetopause-tail current system, *Ann. Geophys.*, *21*, 1709–1722, doi:10.5194/angeo-21-1709-2003.

Burch, J. L., J. Goldstein, P. Mokashi, W. S. Lewis, C. Paty, D. T. Young, A. J. Coates, M. K. Dougherty, and N. Andre (2008), On the cause of Saturn's plasma periodicity, *Geophys. Res. Lett.*, *35*, L14105, doi:10.1029/2008GL034951.

Burch, J. L., A. D. DeJong, J. Goldstein, and D. T. Young (2009), Periodicity in Saturn's magnetosphere: Plasma cam, *Geophys. Res. Lett.*, *36*, L14203, doi:10.1029/2009GL039043.

Burger, M. H., E. C. Sittler, R. E. Johnson, H. T. Smith, O. J. Tucker, and V. I. Shematovich (2007), Understanding the escape of water from Enceladus, *J. Geophys. Res.*, *112*, A06219, doi:10.1029/2006JA012086.

Burke, B., and K. Franklin (1955), Observations of a variable radio source associated with the planet Jupiter, *J. Geophys. Res.*, *60*, 213–217, doi:10.1029/JZ060i002p00213.

Burton, M. E., M. K. Dougherty, and C. T. Russell (2010), Saturn's internal planetary magnetic field, *Geophys. Res. Lett.*, *37*, L24105, doi:10.1029/2010GL045148.

Cao, H., C. T. Russell, U. R. Christensen, M. K. Dougherty, and M. E. Burton (2011), Saturn's very axisymmetric magnetic field: No detectable secular variation or tilt, *Earth Planet. Sci. Lett.*, *304*, 22–28, doi:10.1016/j.epsl.2011.02.035.

Carbary, J. F., and S. M. Krimigis (1982), Charged particle periodicity in the Saturnian magnetosphere, *Geophys. Res. Lett.*, *9*(9), 1073–1076, doi:10.1029/GL009i009p01073.

Carbary, J. F., D. G. Mitchell, S. M. Krimigis, D. C. Hamilton, and N. Krupp (2007a), Charged particle periodicities in Saturn's outer magnetosphere, *J. Geophys. Res.*, *112*, A06246, doi:10.1029/2007JA012351.

Carbary, J. F., D. G. Mitchell, S. M. Krimigis, D. C. Hamilton, and N. Krupp (2007b), Spin-period effects in magnetospheres with no axial tilt, *Geophys. Res. Lett.*, *34*, L18107, doi:10.1029/2007GL030483.

Carbary, J. F., D. G. Mitchell, S. M. Krimigis, and N. Krupp (2007c), Evidence for spiral pattern in Saturn's magnetosphere using the new SKR longitudes, *Geophys. Res. Lett.*, *34*, L13105, doi:10.1029/2007GL030167.

Carbary, J. F., D. G. Mitchell, P. Brandt, C. Paranicas, and S. M. Krimigis (2008), ENA periodicities at Saturn, *Geophys. Res. Lett.*, *35*, L07102, doi:10.1029/2008GL033230.

Carr, T. D., A. C. Smith, R. Pepple, and C. H. Barrow (1958), 18-Megacycle observations of Jupiter in 1957, *Astrophys. J.*, *127*, 274, doi:10.1086/146460.

Carr, T. D., J. J. Schauble, and C. C. Schauble (1981), Pre-encounter distributions of Saturn's low frequency radio emission, *Nature*, *292*, 745–747, doi:10.1038/292745a0.

Cassidy, T. A., and R. E. Johnson (2010), Collisional spreading of Enceladus' neutral cloud, *Icarus*, *209*, 696–703, doi:10.1016/j.icarus.2010.04.010.

Cecconi, B., L. Lamy, P. Zarka, R. Prangé, W. S. Kurth, and P. Louarn (2009), Goniopolarimetric study of the revolution 29 perikrone using the Cassini Radio and Plasma Wave Science instrument high-frequency radio receiver, *J. Geophys. Res.*, *114*, A03215, doi:10.1029/2008JA013830.

Cheng, A. F., and J. H. Waite (1988), Corotation lag of Saturn's magnetosphere: Global ionospheric conductivities revisited, *J. Geophys. Res.*, *93*, 4107–4109, doi:10.1029/JA093iA05p04107.

Clarke, J. T., et al. (2005), Morphological differences between Saturn's ultraviolet aurora and those of Earth and Jupiter, *Nature*, *433*, 717–719, doi:10.1038/nature03331.

Clarke, K. E., D. J. Andrews, A. J. Coates, S. W. H. Cowley, and A. Masters (2010a), Magnetospheric period oscillations of Saturn's bow shock, *J. Geophys. Res.*, *115*, A05202, doi:10.1029/2009JA015164.

Clarke, K. E., D. J. Andrews, C. S. Arridge, A. J. Coates, and S. W. H. Cowley (2010b), Magnetopause oscillations near the planetary period at Saturn: Occurrence, phase, and amplitude, *J. Geophys. Res.*, *115*, A08209, doi:10.1029/2009JA014745.

Connerney, J. E. P. (1993), Magnetic field of the outer planets, *J. Geophys. Res.*, *98*, 18,659–18,679, doi:10.1029/93JE00980.

Connerney, J. E. P., M. H. Acuna, and N. F. Ness (1983), Currents in Saturn's magnetosphere, *J. Geophys. Res.*, *88*, 8779–8789, doi:10.1029/JA088iA11p08779.

Cowley, S. W. H., D. M. Wright, E. J. Bunce, A. C. Carter, M. K. Dougherty, G. Giampieri, J. D. Nichols, and T. R. Robinson (2006), Cassini observations of planetary-period magnetic field oscillations in Saturn's magnetosphere: Doppler shifts and phase motion, *Geophys. Res. Lett.*, *33*, L07104, doi:10.1029/2005GL025522.

Cowley, S. W. H., C. S. Arridge, E. J. Bunce, J. T. Clarke, A. J. Coates, M. K. Dougherty, J. Gérard, D. Grodent, J. D. Nichols, and D. L. Talboys (2008), Auroral current systems in Saturn's magnetosphere: Comparison of theoretical models with Cassini and HST observations, *Ann. Geophys.*, *26*, 2613–2630, doi:10.5194/angeo-26-2613-2008.

Desch, M. D., and M. L. Kaiser (1981), Voyager measurement of the rotation period of Saturn's magnetic field, *Geophys. Res. Lett.*, *8*, 253–256, doi:10.1029/GL008i003p00253.

Dougherty, M. K., et al. (2005), Cassini magnetometer observations during Saturn orbit insertion, *Science*, *307*, 1266–1270, doi:10.1126/science.1106098.

Espinosa, S. A., and M. K. Dougherty (2000), Periodic perturbations in Saturn's magnetic field, *Geophys. Res. Lett.*, *27*, 2785–2788, doi:10.1029/2000GL000048.

Espinosa, S. A., D. J. Southwood, and M. K. Dougherty (2003), How can Saturn impose its rotation period in a noncorotating magnetosphere?, *J. Geophys. Res.*, *108*(A2), 1086, doi:10.1029/2001JA005084.

Fleshman, B. L., P. A. Delamere, and F. Bagenal (2010), A sensitivity study of the Enceladus torus, *J. Geophys. Res.*, *115*, E04007, doi:10.1029/2009JE003372.

Fukazawa, K., S. Ogi, T. Ogino, and R. J. Walker (2007), Magnetospheric convection at Saturn as a function of IMF B$_Z$, *Geophys. Res. Lett.*, *34*, L01105, doi:10.1029/2006GL028373.

Galopeau, P. H. M., and A. Lecacheux (2000), Variations of Saturn's radio rotation period measured at kilometer wavelengths, *J. Geophys. Res.*, *105*, 13,089–13,102, doi:10.1029/1999JA005089.

Galopeau, P., P. Zarka, and D. Le Queau (1989), Theoretical model of Saturn's kilometric radiation spectrum, *J. Geophys. Res.*, *94*, 8739–8755, doi:10.1029/JA094iA07p08739.

Goldreich, P., and A. J. Farmer (2007), Spontaneous axisymmetry breaking of the external magnetic field at Saturn, *J. Geophys. Res.*, *112*, A05225, doi:10.1029/2006JA012163.

Gombosi, T. I., and K. C. Hansen (2005), Saturn's variable magnetosphere, *Science*, *307*, 1224–1226, doi:10.1126/science.1108226.

Gombosi, T. I., G. Tóth, D. L. de Zeeuw, K. C. Hansen, K. Kabin, and K. G. Powell (2002), Semi-relativistic magnetohydrodynamics and physics-based convergence acceleration, *J. Comput. Phys.*, *177*, 176–205, doi:10.1006/jcph.2002.7009.

Gombosi, T. I., et al. (2004), Solution-adaptive magnetohydrodynamics for space plasmas: Sun-to-Earth simulations, *Comput. Sci. Eng.*, *6*(2), 14–35, doi:10.1109/MCISE.2004.1267603.

Gombosi, T. I., T. P. Armstrong, C. S. Arridge, K. K. Khurana, S. M. Krimigis, N. Krupp, A. M. Persoon, and M. F. Thomsen (2009), Saturn's magnetospheric configuration, in *Saturn from Cassini-Huygens*, edited by M. K. Dougherty, L. W. Esposito, and S. M. Krimigis, pp. 203–255, Springer, New York, doi:10.1007/978-1-4020-9217-6_9.

Gurnett, D. A., et al. (2005), Radio and plasma wave observations at Saturn from Cassini's approach and first orbit, *Science*, *307*, 1255–1259, doi:10.1126/science.1105356.

Gurnett, D. A., A. M. Persoon, W. S. Kurth, J. B. Groene, T. F. Averkamp, M. K. Dougherty, and D. J. Southwood (2007), The variable rotation period of the inner region of Saturn's plasma disk, *Science*, *316*(5823), 442–445, doi:10.1126/science.1138562.

Gurnett, D. A., A. M. Persoon, J. B. Groene, A. J. Kopf, G. B. Hospodarsky, and W. S. Kurth (2009a), A north-south difference in the rotation rate of auroral hiss at Saturn: Comparison to Saturn's kilometric radio emission, *Geophys. Res. Lett.*, *36*, L21108, doi:10.1029/2009GL040774.

Gurnett, D. A., A. Lecacheux, W. S. Kurth, A. M. Persoon, J. B. Groene, L. Lamy, P. Zarka, and J. F. Carbary (2009b), Discovery of a north-south

asymmetry in Saturn's radio rotation period, *Geophys. Res. Lett.*, *36*, L16102, doi:10.1029/2009GL039621.

Gurnett, D. A., J. B. Groene, A. M. Persoon, J. D. Menietti, S.-Y. Ye, W. S. Kurth, R. J. MacDowall, and A. Lecacheux (2010), The reversal of the rotational modulation rates of the north and south components of Saturn kilometric radiation near equinox, *Geophys. Res. Lett.*, *37*, L24101, doi:10.1029/2010GL045796.

Hansen, K. C., T. I. Gombosi, D. Dezeeuw, C. P. T. Groth, and K. G. Powell (2000), A 3D global MHD simulation of Saturn's magnetosphere, *Adv. Space Res.*, *26*, 1681–1690, doi:10.1016/S0273-1177(00)00078-8.

Hansen, K. C., A. J. Ridley, G. B. Hospodarsky, N. Achilleos, M. K. Dougherty, T. I. Gombosi, and G. Tóth (2005), Global MHD simulations of Saturn's magnetosphere at the time of Cassini approach, *Geophys. Res. Lett.*, *32*, L20S06, doi:10.1029/2005GL022835.

Hansen, C. J., L. Esposito, A. I. F. Stewart, J. Colwell, A. Hendrix, W. Pryor, D. Shemansky, and R. West (2006), Enceladus' water vapor plume, *Science*, *311*, 1422–1425, doi:10.1126/science.1121254.

Hill, T. W., et al. (2008), Plasmoids in Saturn's magnetotail, *J. Geophys. Res.*, *113*, A01214, doi:10.1029/2007JA012626.

Hu, Y. Q., X. C. Guo, and C. Wang (2007), On the ionospheric and reconnection potentials of the Earth: Results from global MHD simulations, *J. Geophys. Res.*, *112*, A07215, doi:10.1029/2006JA012145.

Jackman, C. M., N. Achilleos, E. J. Bunce, B. Cecconi, J. T. Clarke, S. W. H. Cowley, W. S. Kurth, and P. Zarka (2005), Interplanetary conditions and magnetospheric dynamics during the Cassini orbit insertion flythrough of Saturn's magnetosphere, *J. Geophys. Res.*, *110*, A10212, doi:10.1029/2005JA011054.

Jackman, C. M., C. T. Russell, D. J. Southwood, C. S. Arridge, N. Achilleos, and M. K. Dougherty (2007), Strong rapid dipolarizations in Saturn's magnetotail: In situ evidence of reconnection, *Geophys. Res. Lett.*, *34*, L11203, doi:10.1029/2007GL029764.

Jackman, C. M., et al. (2008), A multi-instrument view of tail reconnection at Saturn, *J. Geophys. Res.*, *113*, A11213, doi:10.1029/2008JA013592.

Jackman, C. M., L. Lamy, M. P. Freeman, P. Zarka, B. Cecconi, W. S. Kurth, S. W. H. Cowley, and M. K. Dougherty (2009), On the character and distribution of lower-frequency radio emissions at Saturn and their relationship to substorm-like events, *J. Geophys. Res.*, *114*, A08211, doi:10.1029/2008JA013997.

Jackman, C. M., J. A. Slavin, and S. W. H. Cowley (2011), Cassini observations of plasmoid structure and dynamics: Implications for the role of magnetic reconnection in magnetospheric circulation at Saturn, *J. Geophys. Res.*, *116*, A10212, doi:10.1029/2011JA016682.

Jurac, S., and J. D. Richardson (2005), A self-consistent model of plasma and neutrals at Saturn: Neutral cloud morphology, *J. Geophys. Res.*, *110*, A09220, doi:10.1029/2004JA010635.

Khurana, K. K., D. G. Mitchell, C. S. Arridge, M. K. Dougherty, C. T. Russell, C. Paranicas, N. Krupp, and A. J. Coates (2009), Sources of rotational signals in Saturn's magnetosphere, *J. Geophys. Res.*, *114*, A02211, doi:10.1029/2008JA013312.

Krimigis, S. M., N. Sergis, D. G. Mitchell, D. C. Hamilton, and N. Krupp (2007), A dynamic, rotating ring current around Saturn, *Nature*, *450*, 1050–1053, doi:10.1038/nature06425.

Kurth, W. S., A. Lecacheux, T. F. Averkamp, J. B. Groene, and D. A. Gurnett (2007), A Saturnian longitude system based on a variable kilometric radiation period, *Geophys. Res. Lett.*, *34*, L02201, doi:10.1029/2006GL028336.

Kurth, W. S., T. F. Averkamp, D. A. Gurnett, J. B. Groene, and A. Lecacheux (2008), An update to a Saturnian longitude system based on kilometric radio emissions, *J. Geophys. Res.*, *113*, A05222, doi:10.1029/2007JA012861.

Lamy, L. (2011), Variability of southern and northern SKR periodicities, in *Planetary Radio Emissions VII*, edited by H. O. Rucker et al., pp. 38–50, Austrian Acad. of Sci. Press, Vienna.

Lamy, L., B. Cecconi, R. Prangé, P. Zarka, J. D. Nichols, and J. T. Clarke (2009), An auroral oval at the footprint of Saturn's kilometric radio sources, co-located with the UV aurorae, *J. Geophys. Res.*, *114*, A10212, doi:10.1029/2009JA014401.

Lecacheux, A., P. Galopeau, and M. Aubier (1997), Re-visiting Saturnian radiation with Ulysses/URAP, in *Planetary Radio Emissions IV*, edited by H. O. Rucker, S. J. Bauer, and A. Lecacheux, pp. 313–325, Austrian Acad. of Sci. Press, Vienna.

Lyon, J. G., J. A. Fedder, and C. M. Mobarry (2004), The Lyon–Fedder–Mobarry (LFM) global MHD magnetospheric simulation code, *J. Atmos. Sol. Terr. Phys.*, *66*, 1333–1350, doi:10.1016/j.jastp.2004.03.020.

Masters, A., et al. (2010), Cassini observations of a Kelvin Helmholtz vortex in Saturn's outer magnetosphere, *J. Geophys. Res.*, *115*, A07225, doi:10.1029/2010JA015351.

Mitchell, D. G., et al. (2009a), Recurrent energization of plasma in the midnight-to-dawn quadrant of Saturn's magnetosphere, and its

relationship to auroral UV and radio emissions, *Planet. Space Sci.*, *57*, 1732–1742, doi:10.1016/j.pss.2009.04.002.

Mitchell, D. G., J. F. Carbary, S. W. H. Cowley, T. W. Hill, and P. Zarka (2009b), The dynamics of Saturn's magnetosphere, in *Saturn From Cassini-Huygens*, edited by M. K. Dougherty, L. W. Esposito, and S. M. Krimigis, pp. 257–279, Springer, New York, doi:10.1007/978-1-4020-9217-6_10.

Moore, L., I. Mueller-Wodarg, M. Galand, A. Kliore, and M. Mendillo (2010), Latitudinal variations in Saturn's ionosphere: Cassini measurements and model comparisons, *J. Geophys. Res.*, *115*, A11317, doi:10.1029/2010JA015692.

Müller-Wodarg, I. C. F., M. Mendillo, R. V. Yelle, and A. D. Aylward (2006), A global circulation model of Saturn's thermosphere, *Icarus*, *180*, 147–160, doi:10.1016/j.icarus.2005.09.002.

Paranicas, C., D. G. Mitchell, E. C. Roelof, P. C. Brandt, D. J. Williams, S. M. Krimigis, and B. H. Mauk (2005), Periodic intensity variations in global ENA images of Saturn, *Geophys. Res. Lett.*, *32*, L21101, doi:10.1029/2005GL023656.

Powell, K. G., P. L. Roe, T. J. Linde, T. I. Gombosi, and D. L. DeZeeuw (1999), A solution-adaptive upwind scheme for ideal magnetohydrodynamics, *J. Comput. Phys.*, *154*, 284–309, doi:10.1006/jcph.1999.6299.

Provan, G., D. J. Andrews, C. S. Arridge, A. J. Coates, S. W. H. Cowley, S. E. Milan, M. K. Dougherty, and D. M. Wright (2009a), Polarization and phase of planetary-period magnetic field oscillations on high-latitude field lines in Saturn's magnetosphere, *J. Geophys. Res.*, *114*, A02225, doi:10.1029/2008JA013782.

Provan, G., S. W. H. Cowley, and J. D. Nichols (2009b), Phase relation of oscillations near the planetary period of Saturn's auroral oval and the equatorial magnetospheric magnetic field, *J. Geophys. Res.*, *114*, A04205, doi:10.1029/2008JA013988.

Provan, G., D. J. Andrews, B. Cecconi, S. W. H. Cowley, M. K. Dougherty, L. Lamy, and P. M. Zarka (2011), Magnetospheric period magnetic field oscillations at Saturn: Equatorial phase "jitter" produced by superposition of southern and northern period oscillations, *J. Geophys. Res.*, *116*, A04225, doi:10.1029/2010JA016213.

Provan, G., D. J. Andrews, C. S. Arridge, A. J. Coates, S. W. H. Cowley, G. Cox, M. K. Dougherty, and C. M. Jackman (2012), Dual periodicities in planetary-period magnetic field oscillations in Saturn's tail, *J. Geophys. Res.*, *117*, A01209, doi:10.1029/2011JA017104.

Raeder, J., J. Berchem, and M. Ashour-Abdalla (1998), The Geospace Environment Modeling Grand Challenge: Results from a Global Geospace Circulation Model, *J. Geophys. Res.*, *103*(A7), 14,787, doi:10.1029/98JA00014.

Richardson, J. D., A. Eviatar, M. A. McGrath, and V. M. Vasyliũnas (1998), OH in Saturn's magnetosphere: Observations and implications, *J. Geophys. Res.*, *103*(E9), 20,245–20,255, doi:10.1029/98JE01127.

Ridley, A. J., K. C. Hansen, G. Tóth, D. L. De Zeeuw, T. I. Gombosi, and K. G. Powell (2002), University of Michigan MHD results of the Geospace Global Circulation Model metrics challenge, *J. Geophys. Res.*, *107*(A10), 1290, doi:10.1029/2001JA000253.

Ridley, A., T. I. Gombosi, and D. DeZeeuw (2004), Ionospheric control of the magnetosphere: Conductance, *Ann. Geophys.*, *22*, 567–584, doi:10.5194/angeo-22-567-2004.

Sánchez-Lavega, A., R. Huesoa, S. Pérez-Hoyos, J. F. Rojas, and R. G. French (2004), Saturn's cloud morphology and zonal winds before the Cassini encounter, *Icarus*, *170*, 519–523, doi:10.1016/j.icarus.2004.05.002.

Sánchez-Lavega, A., R. Hueso, and S. Pérez-Hoyos (2007), The three-dimensional structure of Saturn's equatorial jet at cloud level, *Icarus*, *187*, 510–519, doi:10.1016/j.icarus.2006.10.022.

Sandel, B. R., and A. J. Dessler (1988), Dual periodicity of the jovian magnetosphere, *J. Geophys. Res.*, *93*, 5487–5504, doi:10.1029/JA093iA06p05487.

Seidelmann, P. K., et al. (2002), Report of the IAU/IAG working group on cartographic coordinates and rotational elements of the planets and satellites: 2000, *Celestial Mech. Dyn. Astron.*, *82*, 83–111, doi:10.1023/A:1013939327465.

Shain, C. A. (1955), Location on Jupiter of a source of radio noise, *Nature*, *176*, 836–837, doi:10.1038/176836a0.

Sittler, E. C., Jr., et al. (2008), Ion and neutral sources and sinks within Saturn's inner magnetosphere: Cassini results, *Planet. Space Sci.*, *56*, 3–18, doi:10.1016/j.pss.2007.06.006.

Smith, C. G. A. (2006), Periodic modulation of gas giant magnetospheres by the neutral upper atmosphere, *Ann. Geophys.*, *24*, 2709–2717, doi:10.5194/angeo-24-2709-2006.

Smith, C. G. A. (2011), A Saturnian cam current system driven by asymmetric thermospheric heating, *Mon. Not. R. Astron. Soc.*, *410*, 2315, doi:10.1111/j.1365-2966.2010.17602.x.

Smith, E. J., L. Davis Jr., D. E. Jones, P. J. Coleman Jr., D. S. Colburn, P. Dyal, and C. P. Sonett (1975), Jupiter's magnetic field, magnetosphere,

and interaction with the solar wind-Pioneer 11, *Science*, *188*, 451–455, doi:10.1126/science.188.4187.451.

Smith, H. T., R. E. Johnson, M. E. Perry, D. G. Mitchell, R. L. McNutt, and D. T. Young (2010), Enceladus plume variability and the neutral gas densities in Saturn's magnetosphere, *J. Geophys. Res.*, *115*, A10252, doi:10.1029/2009JA015184.

Southwood, D. (2011), Direct evidence of differences in magnetic rotation rate between Saturn's northern and southern polar regions, *J. Geophys. Res.*, *116*, A01201, doi:10.1029/2010JA016070.

Southwood, D. J., and M. G. Kivelson (2007), Saturnian magnetospheric dynamics: Elucidation of a camshaft model, *J. Geophys. Res.*, *112*, A12222, doi:10.1029/2007JA012254.

Southwood, D. J., and M. G. Kivelson (2009), The source of Saturn's periodic radio emission, *J. Geophys. Res.*, *114*, A09201, doi:10.1029/2008JA013800.

Stevenson, D. J. (2006), Planetary science: A new spin on Saturn, *Nature*, *441*, 34–35, doi:10.1038/441034a.

Thomas, N., F. Bagenal, T. W. Hill, and J. K. Wilson (2004), The Io neutral clouds and plasma torus, in *Jupiter: The Planet, Satellites and Magnetosphere*, edited by F. Bagenal, T. E. Dowling, and W. B. McKinnon, pp. 561–592, Cambridge Univ. Press, Cambridge, U. K.

Thomsen, M. F., D. B. Reisenfeld, D. M. Delapp, R. L. Tokar, D. T. Young, F. J. Crary, E. C. Sittler, M. A. McGraw, and J. D. Williams (2010), Survey of ion plasma parameters in Saturn's magnetosphere, *J. Geophys. Res.*, *115*, A10220, doi:10.1029/2010JA015267.

Tóth, G., et al. (2005), Space Weather Modeling Framework: A new tool for the space science community, *J. Geophys. Res.*, *110*, A12226, doi:10.1029/2005JA011126.

Tóth, G., et al. (2012), Adaptive numerical algorithms in space weather modeling, *J. Comput. Phys.*, *231*, 870–903, doi:10.1016/j.jcp.2011.02.006.

Vasyliūnas, V. M. (1983), Plasma distribution and flow, in *Physics of the Jovian Magnetosphere*, edited by A. Dessler, pp. 395–453, Cambridge Univ. Press, New York, doi:10.1017/CBO9780511564574.013.

Vasyliūnas, V. M. (1994), Role of plasma acceleration time in the dynamics of the Jovian magnetosphere, *Geophys. Res. Lett.*, *21*(6), 401–404, doi:10.1029/94GL00192.

Warwick, J. W., et al. (1981), Planetary radio astronomy observations from Voyager 1 near Saturn, *Science*, *212*, 239–243, doi:10.1126/science.212.4491.239.

Wu, C. S., and L. C. Lee (1979), A theory of the terrestrial kilometric radiation, *Astrophys. J.*, *230*, 621–626, doi:10.1086/157120.

Ye, S.-Y., D. A. Gurnett, J. B. Groene, Z. Wang, and W. S. Kurth (2010), Dual periodicities in the rotational modulation of Saturn narrowband emissions, *J. Geophys. Res.*, *115*, A12258, doi:10.1029/2010JA015780.

Yu, Z. J., and C. T. Russell (2009), Rotation period of Jupiter from the observation of its magnetic field, *Geophys. Res. Lett.*, *36*, L20202, doi:10.1029/2009GL040094.

Zarka, P., L. Lamy, B. Cecconi, R. Prange, and H. O. Rucker (2007), Modulation of Saturn's radio clock by solar wind speed, *Nature*, *450*, 265–267, doi:10.1038/nature06237.

Zieger, B., K. C. Hansen, T. I. Gombosi, and D. L. DeZeeuw (2010), Periodic plasma escape from the mass-loaded Kronian magnetosphere, *J. Geophys. Res.*, *115*, A08208, doi:10.1029/2009JA014951.

T. I. Gombosi and X. Jia, Department of Atmospheric, Oceanic and Space Sciences, University of Michigan, 2455 Hayward St., Ann Arbor, MI 48109-2143, USA. (xzjia@umich.edu)

M. G. Kivelson, Department of Earth and Space Sciences, University of California, 405 Hilgard Ave., 3845 Slichter Hall, PO Box 951567, Los Angeles, CA 90095-1567, USA. (mkivelson@igpp.ucla.edu)